Utrecht University

Department of Physics

Bachelor Thesis

Remco de Smit

Calibration of a digital Forward Calorimeter (FoCal) prototype

Supervisors:

Prof. Dr. T. Peitzmann
Institute for subatomic physics
Utrecht University

Dr. ing. N. van der Kolk
Institute for subatomic physics
Utrecht University

10 June 2019

Abstract

The Forward Calorimeter (FoCal) prototype, which is a digital pixel sensor calorimeter, is made up of absorbing material and active volumes. In the active volumes three different types of chips have been implemented which differ in sensitivity. The differences in sensitivity have been corrected by carrying out a calibration procedure. The calibration procedure is applied to SPS measurements with particle beams of respectively an energy E of 30, 50, 100 and 244 GeV. As a result 96 calibration factors are attained. The calibration factors are applied to the raw data to obtain calibrated longitudinal hit profiles.

Contents

1 Introduction

1.1 Quantum Chromo Dynamics

Physicists have done a lot of research over the last century to obtain a better insight into the fundamental structure of matter. This research lead to the remarkable conclusion that our universe is made up of elementary particles, governed by four fundamental forces. How the electromagnetic, strong and weak interaction are related to these elementary particles is described by the Standard Model. Elementary particles can be divided into two groups: quarks and leptons. Quarks are the building blocks of hadrons, which can build up the nucleons of atoms (protons, neutrons). Quarks are spin-$\frac{1}{2}$ particles, which can have six different flavours: up, down, charm, strange, top or bottom. The flavours are divided in three generations, up and down form a generation (I), charm and strange form a generation (II) and top and bottom form a generation (III). Quarks in higher generations have higher masses. The up, charm and top quark have an electrical charge of $+\frac{2}{3}$. The down, strange and bottom quark have an electrical charge of $-\frac{1}{3}$ [1–3].

According to *Quantum Chromo Dynamics* (QCD) quarks carry colour charge, which states that a quark of a certain flavour can have three different colour states with equal masses and electroweak charges. The interaction between these quarks, induced by the colour charge, is called the strong interaction. Quarks and gluons are *confined* inside hadrons: no free quarks and gluons can be found in nature, just the colour neutral composite states. The colour charge is confined to spatial regions of roughly the size of hadrons. On the other hand, the coupling constant between quarks and gluons becomes progressively weaker at smaller distances and increasing energy, where they are almost free and only interact weakly with each other. This phenomenon is known as *asymptotic freedom*. In high energy nuclear collisions energy densities of several GeV/fm^3 are reachable. Looking at the phase diagram of QCD, energy density scales like that bring the hadronic matter in a phase where the long-ranged confining potential disappears and the coupling of QCD decreases. The quarks and gluons enter a deconfined phase where the quarks become free over a large volume. This state of matter is called the *Quark Gluon Plasma* [4–6].

To understand particle production in high-energy hadron collisions, it is of utmost importance to have knowledge of the density of quarks and gluons inside a nucleon. Furthermore, to make predictions for the Standard Model and beyond Standard Model processes it is important to have knowledge of the Parton Distribution Functions (PDFs). Since quarks and gluons are building blocks of hadrons, a varying fraction of the total momentum of the hadron can be carried by each of them and this momentum fraction is given by Bjorken x [7]:

$$x = \frac{p_{constituent}}{p_{hadron}}. \tag{1.1}$$

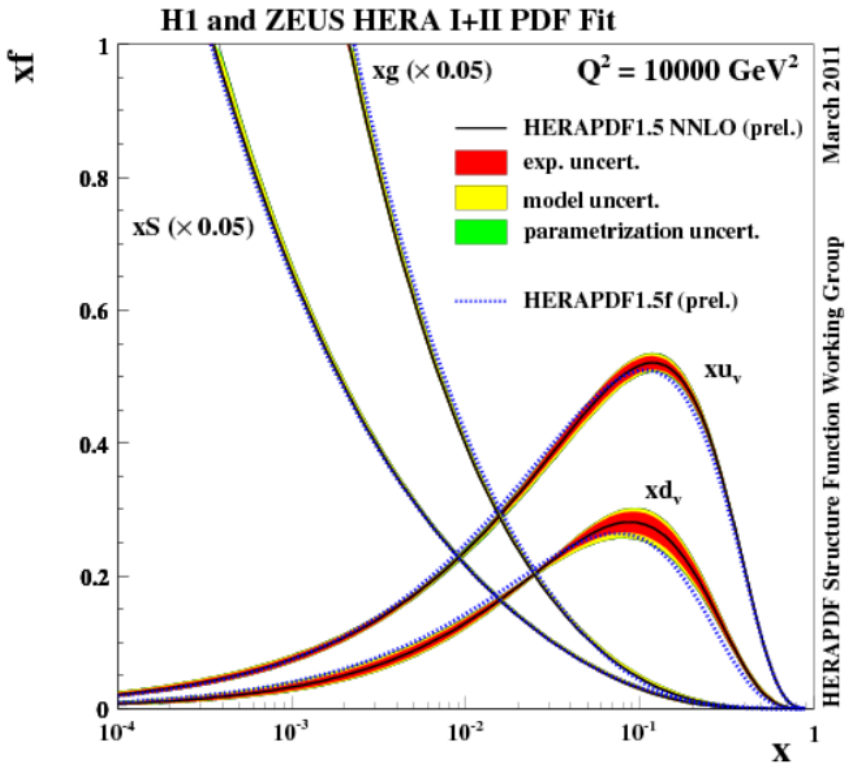

Figure 1.1: Parton Distribution Function (PDF) ,which gives the probability of finding a parton with momentum fraction x, given for a momentum transfer of $Q^2 = 10000$ GeV^2 [8]. As can be seen the number of gluons increases exponentially for decreasing x. The data is taken from HERA (Hadron-Electron Ring Accelerator) at DESY.

The probability of finding a parton with momentum fraction x is given by the Parton Distribution Function, which is also a function of the momentum transfer Q^2 involved in the interaction with the hadron. The evolution of the PDFs can be described by the DGLAP[1] equation [5, 8].

According to the DGLAP evolution equation the gluon density increases with Q^2 and $1/x$. At low x and high Q^2 this yields very high gluon densities. As a consequence an ever growing number of gluons is predicted, which will lead to unitarity violation. At these high gluon densities non-linear processes become important which can no longer be described by the DGLAP evolution equation. One of these processes is gluon overlapping, which could possibly make them merge. As a consequence the number of gluons stabilizes and saturates. The state of gluon matter that arises then is called the *Colour Glass Condensate* (CGC). For even lower x one finds higher gluon densities, which could lead to gluon saturation. The gluon saturation starts below a certain momentum Q^2, which is called the *saturation scale* (Q_s):

$$Q_s^2 \propto A^{\frac{1}{3}} x^{-\lambda}. \tag{1.2}$$

[1]The DGLAP evolution equation is named after the authors who first wrote down the QCD evolution equation. The authors are Y. Dokshitzer, V.N. Gribov, L.N. Lipatov, G. Altarelli and G. Parisi.

Here A is the atomic mass number and x is defined in equation 1.1. Figure 1.1 shows a parton distribution function from which can be obtained that the number of gluons (in this figure scaled down by a factor of 20) increases exponentially for decreasing x [2, 5, 7, 9, 10].

From equation 1.2 it follows that larger nuclei and lower x yield a higher saturation scale and therefore stronger saturation effects. Since the highest sensitivity is obtained at low x, these values are of main interest. The x-values of incoming partons in a high energy collision, can be derived from the final-state kinematics:

$$x \approx \frac{2p_T}{\sqrt{s}} \exp(-y), \tag{1.3}$$

where p_T is the transverse momentum of the outgoing parton, $\sqrt{s}$ is the centre of mass energy and y the rapiditiy of the outgoing parton. Equation 1.3 yields that low values of x can be attained by increasing the centre of mass energy $\sqrt{s}$ or increasing rapidity y. The rapidity is defined as:

$$y = \frac{1}{2} \ln\left(\frac{E + p_L}{E - p_L}\right), \tag{1.4}$$

where p_L is the longitudinal momentum of the parton. In high energy heavy ion physics the rapidity can be well approximated by the pseudorapidity η, which is defined as:

$$\eta = -\ln\left(\tan\left(\frac{\theta}{2}\right)\right), \tag{1.5}$$

where θ is the angle the outgoing particles make with the beam axis. The derivation of the pseudorapidity obtained from the rapidity is given in appendix A. Since low x values are attained by high rapidities and therefore high pseudorapidities, high energy collisions where the outgoing particles have a small angle θ with respect to the beam axis are of main interest. To reach the low x-region, measurements at small polar angles will have to be performed. Measurements at these small polar angles are better known as forward measurements [5, 9, 10].

1.2 FoCal motivation

As was discussed before, the DGLAP evolution equation describes the evolution of PDFs sufficiently at low gluon density scale. At higher gluon densities (and therefore at lower x or higher Q^2) non-linear effects become important and the DGLAP equations no longer suffice. At these high gluon densities gluon saturation start playing a role, which could result in a state of matter better known as the Colour Glass Condensate (CGC). Gluon saturation occurs at low x at a corresponding saturation scale given by 1.2. Experiments in this low x region might obtain better insight into the PDFs at these x values, which at the moment have large experimental uncertainties. Performing measurements on direct photons, which are produced in parton interactions, can provide crucial information in the low x-region of the gluon PDFs [9].

The FoCal (Forward Calorimeter) is introduced as a possible upgrade of ALICE[2] at the LHC[3] at CERN[4]. The FoCal is intended to cover direct photon measurements in the pseudorapidity range $3.2 < \eta < 5.3$. The dominant background of decay photons, which is predominantly caused by neutral pion (π^0) decay, makes it difficult to measure direct photons at these rapidities. Taking the neutral pions at these rapidities into consideration, this means a decay of a neutral pion into two decay photons with a very small opening angle . The main challenge in the detector construction will be to discriminate between the direct photons and the decay photons. As a result the FoCal detector should have a very high spatial resolution, which can be achieved by high granularity.

The (x, Q^2) region covered by different experiments is shown in figure 1.2. The figure shows that the FoCal is intended to measure at low x-values and could provide better insight in gluon saturation effects [9, 10].

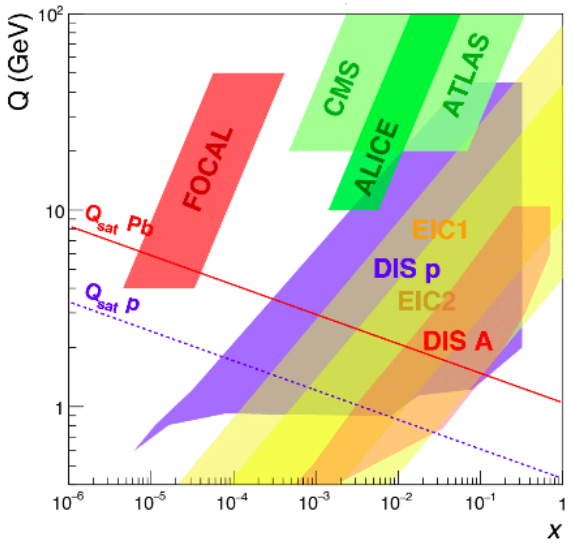

Figure 1.2: Coverage of the (x, Q^2) region for different Deep Inelastic Scattering (DIP) and forward measurement experiments at the Large Hadron Collider (LHC) [9].

[2]ALICE = A Large Hadron Collider Experiment
[3]LHC = Large Hadron Collider
[4]CERN = Conseil Européen pour la Recherche Nucléaire

2 Calorimetry

In particle physics, calorimetry is an omnipresent principle used to measure the energy of primarily electrons, photons and hadrons. Incident particles enter a so-called calorimeter where they deposit their energy and come to a halt, due to interaction processes with the material of the calorimeter. These interaction processes are induced by electromagnetic and strong processes, which cause the incident particle to produce secondary, less energetic particles. Repeating this with the secondary particles and so on, one obtains a shower or cascade of particles. This process will carry on until the energy of the created particles falls below a level where the energy is too little to create more particles. Initially the energy deposition augments in the longitudinal direction of the detector until it reaches a maximum, whereafter it decreases until all the energy of the incident particle is deposited in the detector. Figure 2.1 shows an example of an electromagnetic shower induced by an electron.

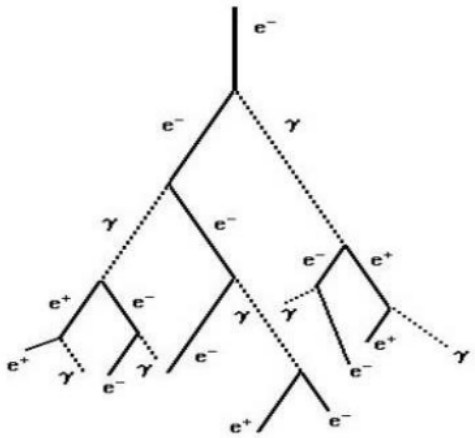

Figure 2.1: A schematic representation of an electromagnetic shower induced by an electron [11].

The calorimeter therefore has to fulfill two tasks. At first the incident particle has to be stopped by causing the particle to deposit its energy in the calorimeter material, secondly it has to generate a measurable quantity which can be converted to the incident energy of the particle traversing the detector. The part that takes care of the energy loss is called the absorber and the part that causes the measurable signal is called the sensor [12].

2.1 Calorimeters

Calorimeters can be roughly sorted into two types. Hadronic calorimeters detect particles that interact mainly via the strong interaction, hadrons. On the other hand electromagnetic calorimeters detect particles that mainly interact via the electromagnetic interaction, leptons and photons. The emphasis of this thesis lies on electromagnetic calorimeters. Therefore whenever a calorimeter is mentioned throughout this thesis, an electromagnetic calorimeter is meant. Calorimeters can be further classified by their construction. Homogeneous calorimeters consist of one type of material, which absorbs the energy of the particle and also takes care of generating a measurable signal. Sampling calorimeters on the other hand

have such a construction that layers of absorbing material are alternated with active volumes that generate the signals. Sampling calorimeters can be constructed such that each material fulfills its task optimally, which might also be financially beneficial. The energy resolution of a homogeneous calorimeter is in general better since all the energy is deposited in the active volume [12].

Particles entering a calorimeter produce a cascade or a shower of secondary, less energetic particles as was discussed at the start of this chapter. The energy degradation is caused by several processes which each have a different impact on the shower development. An electromagnetic shower has a composition of a multitude of electrons, positrons and photons. The charged particles (electrons, positrons) interact differently with matter than photons, so a discrimination between these two groups has to be made when examining the energy loss processes.

Electrons and positrons mainly lose energy through:

- Bremsstrahlung
- Ionization
- Scintillation photons
- Cherenkov photons

Photons mainly lose energy through:

- Pair production
- Compton scattering
- Photoelectric effect
- Rayleigh scattering

In figure 2.2 the fractional energy loss per radiation length (X_0 (see section 2.4) is given for the different energy degradation processes as a function of the electron or positron energy. It becomes clear that for energies above $\sim$ 10 MeV bremsstrahlung is dominant. For energies below $\sim$ 10 MeV charged particles mainly lose energy through ionisation[13].
The different energy loss processes for electrons and positrons on the one hand and photons on the other hand will be discussed in the subsections 2.2, 2.3. The properties of electromagnetic showers will be discussed in 2.4. The different subsections are based on [5, 12–16].

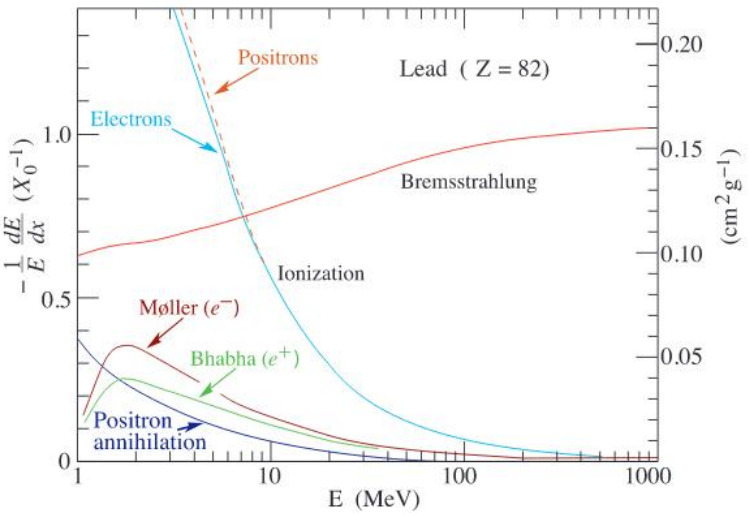

Figure 2.2: The fractional energy loss per radation length (X_0) (see section 2.4) is plotted against the energy of the electron or positron [13]. In the lower energy region ionization is the dominant energy deposition process, whereas in the higher energy domain bremsstrahlung dominates.

2.2 Energy loss of electrons and positrons

The energy loss of electrons and positrons is induced by the electromagnetic interaction. The electrons and positrons pass through the matter and interact by ionizing the atoms inside the matter, provided that the energy of the charged particles is large enough. When this condition fails, the particles might still excite the atoms. The different energy loss processes are discussed below.

2.2.1 Bremsstrahlung

Figure 2.2 shows that Bremsstrahlung is the dominant energy loss process for electrons and positrons of energies above $\sim$ 10 MeV. Charged particles passing through an electric field might be deflected and therefore decelerated by this electric field. As a consequence the particle's energy decreases and this energy lost is converted into photon radiation, which is called Bremsstrahlung.

2.2.2 Ionization

Charged particles possess the ability to ionize atoms in the detector material as the electromagnetic interaction causes energy losses when passing through matter. In the ionization process one or more electrons gain enough energy to escape the Coulomb field of the atom, which leaves the atom ionized. The Bethe-Bloch formula describes the energy loss due to ionization and is given by [5, 13]:

$$-\frac{dE}{dx} = Kz^2\frac{Z}{A}\frac{1}{\beta^2}[\frac{1}{2}\ln\frac{2m_e c^2\beta^2\gamma^2 T_{max}}{I^2} - \beta^2 - \frac{\delta}{2}], \tag{2.1}$$

The relevant variables used in equation 2.1 are listed in table 1. T_{max} is defined as the maximum amount of energy lost within a single interaction by an electron.

Variable	Description	Variable	Description
$m_e c^2$	electron rest mass energy	z	charge number incident particle
r_e	electron radius	Z	atomic number absorber
α	fine structure constant	A	atomic mass number
N_A	number of Avogadro	I	mean excitation energy
K	$4\pi N_A r_e^2 m_e c^2$	δ	density effect correction

Table 1: Overview of the variables used in equation 2.1 [13].

Figure 2.3 shows the mass stopping power for muons in copper. From figure 2.2 it can be obtained that ionization is the dominant energy loss process in the lower energy domain ($\sim 1 - 10$ MeV). Looking back at figure 2.3 it is obtained that in this domain the mass stopping power function has a minimum for $\beta\gamma \approx 3$. Particles possessing this momentum can keep this for a quite long time since the energy loss is small. Particles with momenta close to this minimum are called Minimum Ionizing Particles (MIPs).

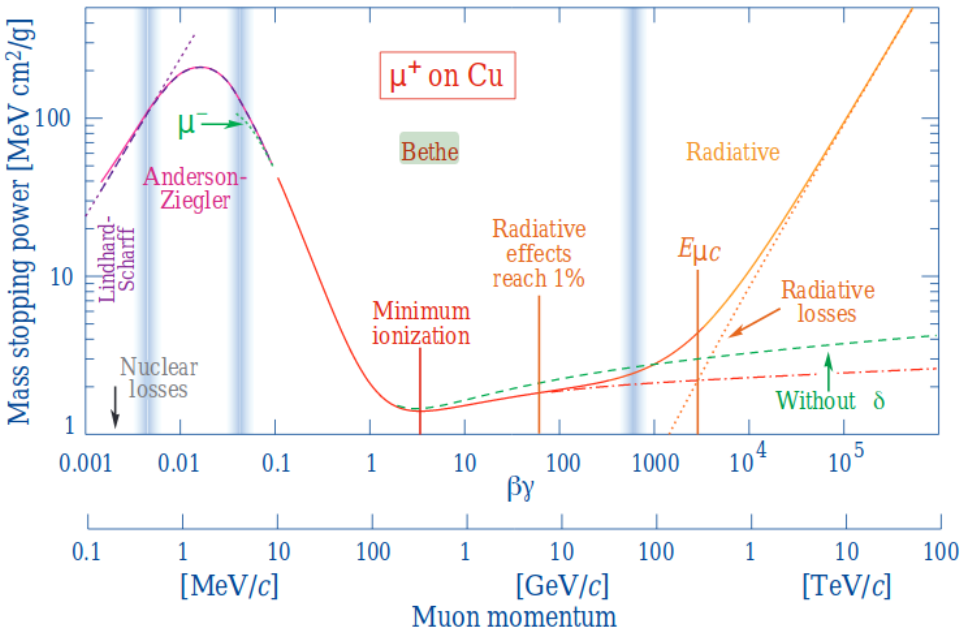

Figure 2.3: The mass stopping power for muons in copper as a function of the momentum p [13]. A minimum in the mass stopping power is found for $\beta\gamma \approx 3$. Particles with momenta close to this minimum are called Minimum Ionizing Particles (MIPs).

2.2.3 Scintillation photons

Scintillation is based on the same principle as ionization. Charged particles passing through matter lose energy through the electromagnetic interaction. When the energy scale of ioniza-

tion is not attained, the energy losses can not be used to ionize atoms. However, the energy scale might be such that atoms get into excited states, which are unstable. The instability causes the atoms in general to fall back to the ground state. The energy release from de-excitation is used to form one or more photons, *scintillation* photons.

2.2.4 Cherenkov photons

When the speed of light in a certain medium is less than a charged particle's velocity passing through that (dielectric) medium, the charged particle radiates photons, *Cherenkov photons*. The electrons in the medium are shifted by the field of the charged particles passing through the medium. The requirement on the velocity of the charged particle is stated as: $v_{ch} \geq \frac{c}{n}$, where $\frac{c}{n}$ gives the speed of light in the medium and n the refractive index of the medium. From figure 2.4 now follows that the opening angle between the charged particle and the shifted electric field of the medium is given by:

$$\cos\theta = \frac{\frac{c}{n}t}{vt} = \frac{1}{\beta n} \tag{2.2}$$

where the definition $\beta = \frac{v}{c}$ is used.

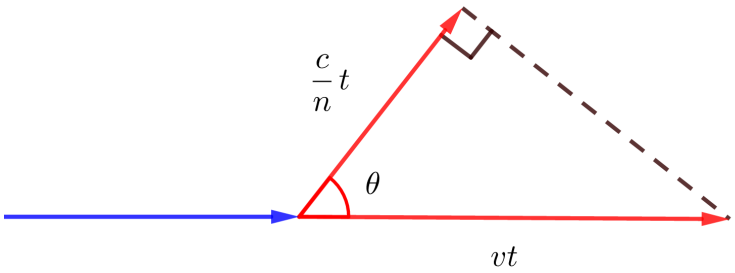

Figure 2.4: The principle of cherenkov radiation for particles with a higher velocity (v) than the speed of light in a certain (dielectric) medium ($\frac{c}{n}$). θ gives the opening angle between the charged particle and the shifted eletric field.

2.3 Interaction of photons

The energy loss of photons is mainly caused by pair production and the photoelectric effect. As can be seen from figure 2.5 the photoelectric effect cross section is dominant in the lower energy region, whereas the cross section of pair production becomes dominant at higher energies. The pair production process obviously comes into account when the energy is at least two times the electron rest mass energy. The different processes causing the energy loss are listed and discussed below.

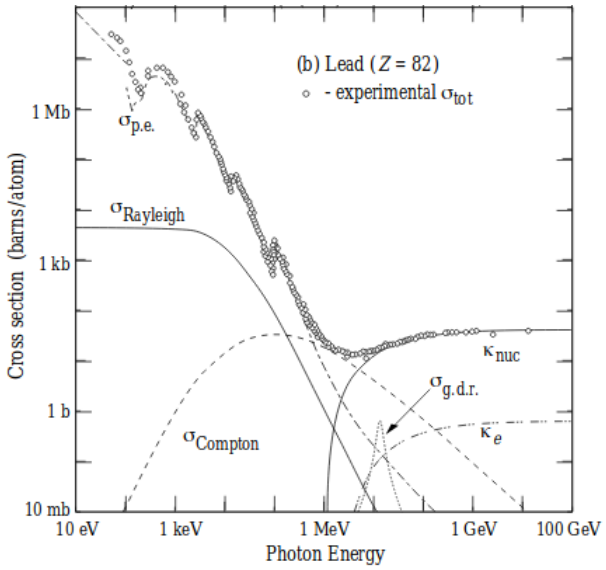

Figure 2.5: The total photon cross sections for different processes as a function of the photon energy in lead. The cross sections for the different processes are discussed in section 2.3 [13]. The processes are labelled in this figure as:
$\sigma_{p.e}$ = Photoelectric effect,
$\sigma_{Rayleigh}$ = Rayleigh scattering,
$\sigma_{Compton}$ = Compton scatteirng,
κ_e and κ_{nuc} = Pair production for respectively nuclear field and electron field.

2.3.1 Pair production

Pair production is the process where a photon in the presence of a charged particle's electric field creates an particle-antiparticle pair. The energy of the incident photon has to be two times the rest energy of the created particle. In the electromagnetic shower case, the incident photon creates in the presence of a charged particle's electric field an electron-positron pair and therefore should at least have twice the electron rest mass energy.

As can be seen from figure 2.5, for energies larger than twice the electron rest mass energy the pair production cross section increases with energy. For energies above 1 GeV the pair production cross section becomes constant. The pair production process becomes dominant for very high energies. The created particles will have a momentum predominantly directed along the incident photon momentum axis and this will continue until the momentum drops to a level where the direction of the created particles significantly changes. Pair production is because of this feature an important process in the beginning of the shower.

2.3.2 Compton scattering

Compton scattering is the process where quasi-free charged particles (electrons in materials (atoms)) gain energy by scattering photons off these free electrons. The free electron gains energy so energy conservation gives a decrease in the photon energy and consequently

frequency. Compton scattering is the dominant energy loss process for energies from a few hundreds of keV till a few MeV in almost all materials.

2.3.3 Photoelectric effect

In the lower energy region the dominant interaction process of photons is the photoelectric effect. In the photoelectric effect process an electron is emitted by an atom through absorption of a photon. This process can also excitate the atom, which brings the atom in an unstable state. When falling back to the ground state, the atom emits Auger electrons or X-rays.

2.3.4 Rayleigh scattering

Unlike the processes mentioned before, Rayleigh scattering does not degrade the energy of the photon. Rayleigh scattering is a process where electrons of atoms in the absorbing material deflect the photon. Since the photons will have a change in direction, the spatial distribution of the deposited energy by the photon (or later created particles) will be affected.

2.4 Electromagnetic shower properties

As was discussed in section 2.1, calorimeters can be divided in two groups: homogeneous and sampling calorimeters. The difference between the two arises in the construction. The calorimeter has to stop the particle and transform the deposited energy into a measurable quantity. It is important to choose material(s) for the construction of the calorimeter that fulfill these tasks optimally. This choice is mainly based on the material properties used inside the calorimeter. The most important ones are the radiation length X_0, the critical energy E_c and the Molière radius R_M.

The radiation length X_0 of a material characterizes the distance the shower has traversed inside the detector and is therefore used as a longitudinal length scale. At high energies the dominant energy loss process is Bremsstrahlung for electrons and positrons and electron-positron pair production is the dominant interaction process for photons. The radiation length X_0 is defined as the distance a high energetic electron traverses until only 1/e of its initial energy is left due to Bremsstrahlung, or for high energetic photons $\frac{7}{9}$ of the mean free path for pair production. The radiation length is given by:

$$X_0 \simeq \frac{716 \cdot A}{Z(Z+1)\ln\frac{287}{\sqrt{Z}}}, \tag{2.3}$$

where Z is the atomic number and A the atomic mass number. The radiation length of a compound or mixture, which has high relevance for sampling calorimeters, can be calculated with:

$$\frac{1}{X_0} = \sum_i \frac{w_i}{X_i}, \tag{2.4}$$

where w_i is the volume fraction and X_i the radiation length of the i-th element in the mixture or compound.

The critical energy is an important parameter in the detector construction, since it is an estimate of the energy level down to which particles will shower. The critical energy E_c is defined as the energy at which the energy loss rate due to Bremsstrahlung equals the energy loss rate of ionization [17]. An alternate definition given by Rossi states that the critical energy E_c is the point at which the energy loss per radiation length due to ionization equals the electron energy [13]. The two definitions are equivalent if the energy loss rate due to Bremsstrahlung is approximated by:$|\frac{dE}{dx}| \approx \frac{E}{X_0}$. In figure 2.6 the two definitions of E_c are given for Copper and it can be obtained that the critical energy of the first definition is slightly larger than Rossi's definition. Furthermore notice the equivalence between Rossi's definition and the first definition if the above approximation for the Bremsstrahlung is made (dashed line).

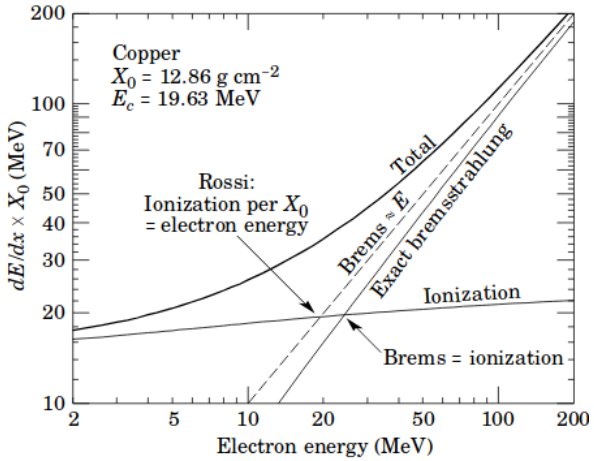

Figure 2.6: Electron energy loss, indicating the cricital energy E_c [13]. Two definitions for the critical energy E_c are shown, where for Rossi's definition an approximation of the energy loss due to Bremsstrahlung might be used. The difference between the two happens to be in the order of a few MeV for Copper.

Due to density effects the ionization loss contributes in a different manner for gases with respect to solids and liquids. Therefore it is difficult to make accurate predictions for the critical energy and a distinction between the two cases is made. The critical energy for solids and liquids is estimated as:[5]

$$E_c = \frac{710\text{MeV}}{Z + 1.24} \tag{2.5}$$

and an estimate of the critical energy for gases is:[5]

$$E_c = \frac{610\text{MeV}}{Z + 0.92} \tag{2.6}$$

where Z is the atomic number.

When highly energetic particles enter the detector, they will interact with the absorber material and produce an electromagnetic shower or cascade due to Bremsstrahlung and pair

production. The number of particles increases until the energy drops below the critical energy E_c, where the main energy loss processes become ionization and excitation. The number of particles therefore increases until it reaches a maximum (shower maximum) and after this maximum the number of particles drops until all the particles are absorbed in the detector. To describe the development of a shower or cascade it is convenient to introduce variables that return the longitudinal distance in units of X_0 and return the energy in terms of E_c:

$$t = \frac{x}{X_0}, y = \frac{E}{E_c}. \tag{2.7}$$

To describe the lateral development of the electromagnetic shower, the Molière radius R_M is used. The Molière radius R_M is defined as:

$$R_M = \frac{X_0 \cdot 21.2(MeV)}{E_c}, \tag{2.8}$$

here the definition of Rossi is used for E_c. A cylinder of radius R_M contains 90% of the energy of the shower and a cylinder of radius $3.5R_M$ contains 99% of the shower energy. Different materials have different radiation lengths and critical energies. The Molière radius of sampling calorimeters which consist of a mixture or compound of different materials can be calculated with:

$$\frac{1}{R_M} = \frac{1}{21.2(MeV)} \sum_i \frac{w_i E_{c,i}}{X_{0,i}}, \tag{2.9}$$

where where w_i is the volume fraction of the material with corresponding critical energy $E_{c,i}$ and radiation length $X_{0,i}$ [13].

For electromagnetic showers the average energy deposition as a function of the longitudinal shower depth t is approximated by a gamma distribution:

$$\frac{dE}{dt} = Eb\frac{(bt)^{\alpha-1}\exp(-bt)}{\Gamma(a)}, \tag{2.10}$$

where a and b are dimensionless parameters. The position of the shower maximum can be obtained from these parameters:

$$t_{max} = \frac{a-1}{b} \tag{2.11}$$

or from the scaled parameter y (indirect from E_c):

$$\begin{aligned} t_{max} &= \ln y + C_i \\ &= \ln \frac{E}{E_c} + C_i. \end{aligned} \tag{2.12}$$

C_i is a constant which has a value of $+0.5$ if the shower is induced by a photon and has a value of -0.5 if the shower is induced by an electron. The longitudinal thickness of the calorimeter to contain 95% of the shower energy is estimated by:

$$t_{95\%} = t_{max} + 0.08Z + 9.6. \tag{2.13}$$

2.5 Energy resolution

In the introduction of this chapter it was stated that a calorimeter has two tasks: stopping the incident particle by making it deposit all its energy inside the detector and generate a signal which is proportional to the energy of the incident particle. In homogeneous calorimeters all the energy is deposited in the active volume which yields a better energy resolution with respect to sampling calorimeters. The energy resolution of a calorimeter is given by:

$$\frac{\sigma_E}{E} = \frac{a}{\sqrt{E}} \oplus \frac{b}{E} \oplus c, \tag{2.14}$$

which can be divided in three terms: $\frac{a}{\sqrt{E}}$ is the stochastic term, $\frac{b}{E}$ is the noise term and c is the constant term. The $\oplus$ indicates a quadratic sum between the terms. From equation 2.14 it follows that each term depends differently on the energy. Therefore the calorimeter technique used for a certain energy range experiment can be significantly different to other experiments. It is important to notice that the different terms in 2.14 might have high absolute values, however relative to each other some of these terms might become negligible or on the other hand terms with small absolute values might become dominant when comparing to the other terms. Below a description of each term in the energy resolution is given, following [12].

Stochastic term: The development of a shower in a detector is a stochastic process. As a consequence the shower development fluctuates and this is where the stochastic term arises. The stochastic term takes intrinsic fluctuations into account. As mentioned before, in homogeneous calorimeters all the energy of the incident particles is deposited in the active volumes. Therefore the shower development has relative small fluctuations for different events and the stochastic terms of these calorimeters are in the order of a few percent (in units of $\frac{1}{\sqrt{E(GeV)}}$).

The stochastic term for sampling calorimeters is due to sampling fluctuations. Since the sampling calorimeters is contructed of alternating layers of absorbing material and active volumes, the measurable energy deposition will be different for different events. The fluctuations in energy deposition are better known as sampling fluctuations. As a result of these sampling fluctuations the number of charged particles that cross layers with active volumes will vary event by event and therefore the signals generated in the active layers too. The number of charged particles crossing the active volumes is in the order of: $N \propto \frac{E_0}{t}$, where E_0 is the incident particle's energy and t is the scaled variable for the longitudinal depth defined in equation 2.7. When crossing the active volumes by charged particles is assumed to be statistically independent, the stochastic term for sampling calorimeters is due to variations in the number of charged particles crossing these layers. The stochastic term is proportional to:

$$\frac{a}{\sqrt{E}} \propto \frac{1}{\sqrt{N}} \propto \sqrt{\frac{t}{E_0(GeV)}}. \tag{2.15}$$

It follows directly from equation 2.15 that taking smaller absorbing layers (and therefore a higher sampling fraction 2.16) yields a better energy resolution. This is explained by the fact that smaller absorbing layers imply a higher number of times that the shower pass through the active volumes and therefore particles passing these active volumes are detected more

often. The stochastic terms for sampling calorimeters are in the order of $5 - 20\%$ (in units of $\frac{1}{\sqrt{E(GeV)}}$).

Noise term: The noise term takes electronic noise into account. This electronic noise arises from the readout chain. When no beam measurements are done with the detector, the detector readout system obtains a random signal generated by the detector which is called the noise. The contribution of the noise term to the energy resolution might become dominant for energies of the incident particles below a few GeV.

The noise contribution for sampling calorimeters can be restricted by increasing the amplitude of the sampling fraction. The sampling fraction f_{samp} is defined as:

$$f_{samp} = \frac{E_{mip}(active)}{E_{mip}(active) + E_{mip}(absorber)}, \tag{2.16}$$

where E_{mip}(active) and E_{mip}(absorber) are the energies deposited respectively in the active volumes and the absorbing volumes by a MIP (minimum-ionizing particle). From equation 2.16 follows that an increase in the sampling fraction results in a higher signal obtained in the active layers and therefore a higher signal-to-noise ratio. A higher degree of the energy will be deposited in the active volumes, so the relative noise contribution decreases. The noise term depends on the factor $\frac{1}{E}$ and is therefore often negligible in th high energy domain.

Constant term: The constant term takes all the energy independent factors to the energy resolution into account. Instrumental effects, such as mechanical imperfections, defects, temperature gradients, detector aging or radiation damage contribute highly to the constant term, as they yield nonuniformities in the detector response. The constant term should be kept in the order of a percent or even less. The reason for this follows from equation 2.14 as for high energies the stochastic and noise term become small. The constant term can become dominant in the high energy domain and therefore has to be kept low.

3 FOCAL

As was discussed in section 1.2 the FoCal detector is proposed as a possible upgrade of the ALICE experiment. The FoCal detector has to cover the pseudorapidity range $3.2 < \eta < 5.3$, which has its consequences for the construction of the detector. At these pseudorapidities the separation angle between particles from a decay or interaction are very small. The FoCal has to be able to separate direct photons and photons from neutral pion decay (π^0), which can be achieved by developing a high granularity detector. Another feature of the detector is the ability to measure jets [7, 10].

The FoCal will be placed at ≈ 7 m from the interaction point and consists of two separate parts, an electromagnetic part (FoCal-E) and a hadronic part (FoCal-H). The objective of the FoCal is to measure photons, so the FoCal-E is of higher importance. Since the focus in this thesis lies on electromagnetic calorimeters, the FoCal-E will be mentioned as FoCal. The FoCal is a hybrid sampling calorimeter which consists of two types of Si-W layers as can be seen from figure 3.1. The tungsten (W) acts as absorber, while the silicon (Si) acts as sensor. The extremely high granularity layers (HGL) take care of the separation between two closeby showers. The HGL have smaller cells than the LGL (higher granularity) and provide therefore an accurate representation of the shower shape. The lower granularity layers (LGL) are added because of their better energy measurement. Figure 3.1 shows the construction of the FoCal detector as it is proposed to improve ALICE [10, 18].

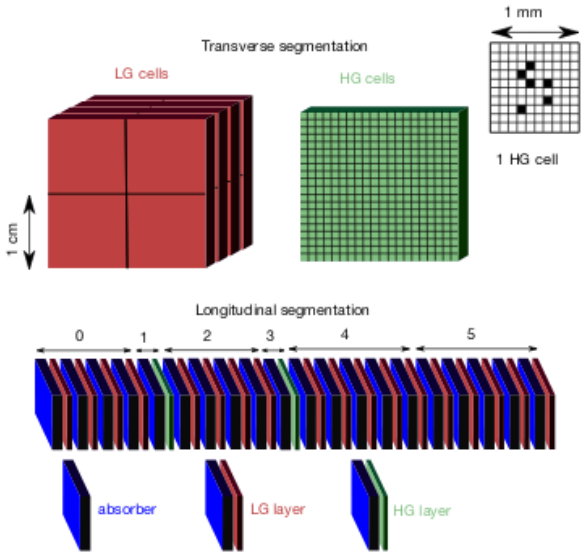

Figure 3.1: Schematic view of the FoCal contruction [19]. The FoCal construction is made up of 24 layers. The construction contains High and Low Granularity Layers, respectively HGL and LGL. The HGLs contribute to a better spatial resolution which is beneficial for two shower separation, while the LGLs contribute to a better measurement of the energy.

In this section the FoCal prototype will be discussed. Beam tests have been done with the FoCal prototype at DESY[5] and with the SPS[6] and PS[7] at CERN. The description of the FoCal prototype follows [19].

3.1 FoCal prototype

The main purpose of the FoCal prototype is to study the principles of a new calorimeter technology and performing measurements with particles in the momentum range from a few GeV/c up to several hundreds of GeV/c. The FoCal prototype is a sampling electromagnetic calorimeter with alternating layers of absorbing material and active volumes generating a signal. The prototype consists of 24 layers, where each layer is made up of an absorber, a silicon sensor, printed circuit boards (PCB) and glue. The PCB provides the data readout.

3.2 Material choice prototype

3.2.1 Absorbing layers

The choice of the absorbing material is based on how the shower develops in the material and depends therefore on the material properties radiation length X_0 and Molière radius R_M. The absorbing material used for the prototype is tungsten, while electromagnetic calorimeters designed before used lead or copper. The material properties of these three materials are listed in table 2:

Material	Density ρ (g$\cdot$ cm^{-3})	Radiation length X_0 (cm)	Molière radius R_M (cm)
Pb	11.35	0.5612	1.602
Cu	8.960	1.436	1.568
W	19.30	0.3504	0.9327

Table 2: Overview of important material properties for the construction of a calorimeter [20]. The properties of lead (Pb), copper (Cu) and tungsten (W) are listed since these materials are of main interest in the material choice as some of them has been used before in electromagnetic calorimeters.

A small Molière radius provides narrow showers in the lateral direction, which is beneficial for two shower separation. Table 2 shows that tungsten has a small Molière radius and radiation length compared to materials used before. The small Molière radius and radiation length are also beneficial for the physical dimensions of the calorimeter. Since the purpose of the detector is making the particles traversing it deposit all their energy inside the detector, a small Molière radius and small radiation length imply smaller dimensions of the prototype [5].

[5]Deutsches Elektronen-Synchrotron
[6]Super Proton Synchotron
[7]Proton Synchotron

3.2.2 Active layers

The type of layers used in the prototype are all high-granularity layers and therefore all have the high-granularity type sensors. These sensors are MIMOSA23 sensors from the IPHC[8]. The sensors are monolithic active pixel sensors (MAPS) based on complementary metal-oxide semiconducter (CMOS) technology. The size of the MIMOSA23 chip is 19.52 mm x 20.93 mm with an active area of 19.52 mm x 19.52 mm. This active area is made up of a grid of 640 x 640 pixels, which themselves have dimensions 30μm x 30μm, which suffices for the digital detector to work.[21]

Figure 3.2a shows the schematic layout of the MIMOSA sensor. The four serializers perform the continous data readout, which runs at 160 MHz. When a particle traverses a pixel, it deposits charge inside the pixel, which is transformed into a bit. The charge is deposited inside the epitaxial layer. Figure 3.2b shows the principle of charge collection inside the pixel. With these small pixel dimensions, very fine sampling of the shower core is possible. In the prototype three different sensors are implemented as not enough sensors of a single type were available. The differences arise in the epitaxial layer resistivity and thickness. The three types are listed in table 3:

	Resistivity (Ω/cm)	Thickness (μm)	# of sensors in prototype
Type 1	10	14	19
Type 2	400	15	46
Type 3	400	20	31

Table 3: Overview of the different types of MIMOSA23 sensors used in the prototype [19]. The resistivity and thickness of the epitaxial layer, as well as the number of sensors in the prototype for each type is indicated.

The choice of tungsten is not only based on its radiation length and Molière radius. The active pixel sensors used in the prototype disperse a significant amount of heat. The heat has to be carried to the outside of the sensor. Since tungsten has a good thermal conductivity ($170W/m/K$), it is able to fulfill this task and cooling elements in the longitudinal direction of the stack are unnecessary. As a consequence the detector can be more compact, which is beneficial for the effective Molière radius. [5]

[8]Institute Pluridisciplinary Hubert Curien

Figure 3.2: Schematic overview of the MIMOSA23 chip.

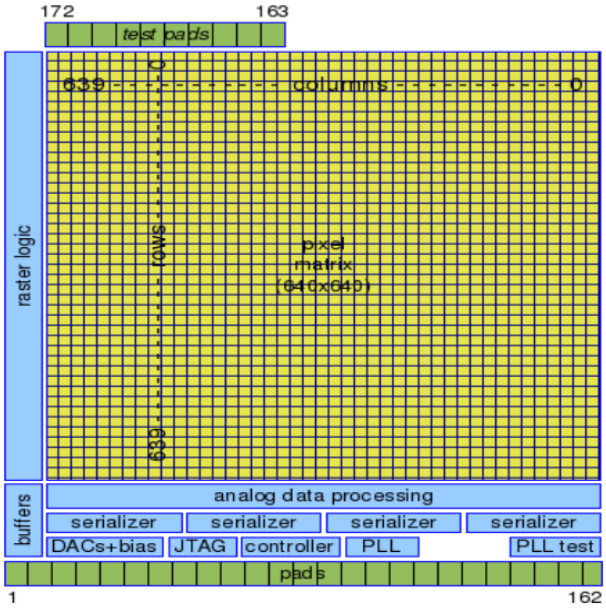

(a) Schematic representation of the MIMOSA23 chip, which is not on scale [21]. The pixel matrix in the middle takes care of the particle detection, since the particle deposits charge inside the pixel which is transformed into a bit.

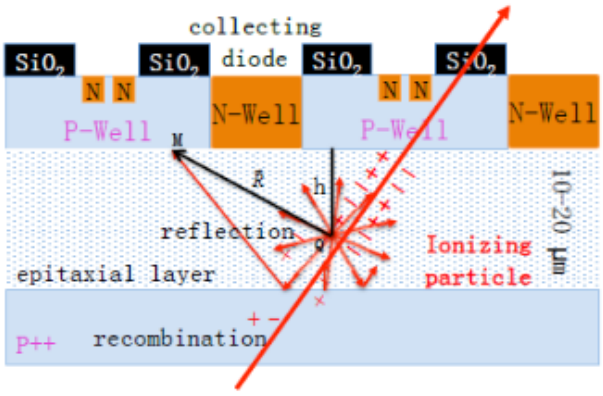

(b) Schematic overview of the charge deposition of a particle inside the epitaxial layer [19]. The charge deposition in the end results in a signal, which is in the form of a bit.

3.3 FoCal prototype

As discussed in the beginning of this section the FoCal prototype consists of 24 layers. Each layer consists of 4 chips, which results in 96 chips in total. Each layer is made up of tungsten, silicon sensors, printed circuit boards (PCB) and glue. It is now possible to derive the radiation length X_0 and the Molière radius of the prototype using equation 2.4 and 2.9 respectively. The radiation length is given by:

$$\begin{aligned}\frac{1}{X_0} &= \frac{V_W}{X_{0,W}} + \frac{V_{Si}}{X_{0,Si}} + \frac{V_{PCB}}{X_{0,PCB}} + \frac{V_{Glue}}{X_{0,Glue}} + \frac{V_{Air}}{X_{0,Air}} \\ &= \frac{0.846}{3.5mm} + \frac{0.031}{93.6mm} + \frac{0.041}{167.6mm} + \frac{0.038}{400mm} + \frac{0.044}{303900mm} \\ &= \frac{1}{4.126mm}\end{aligned} \tag{3.1}$$

Performing an equivalent calculation for the Molière radius, a value of $R_M = 10.5$ mm is obtained. The total thickness of one layer is 4 mm. Relating this to the radiation length in equation 3.1, it follows directly that one layer has a thickness of $0.97X_0$.[18]

The layers consist of active volumes and absorbing volumes. The active volumes have an area of 40x40 mm^2 and the active volumes are made up of four sensors. The absorbing volumes have an area of 50x50 mm^2. Considering the Mollère radius of the detector, it can be concluded that the detector is able to fully contain showers in the lateral direction. In the longitudinal direction the depth of the stack to contain 95% of the shower energy is given by equation 2.13. Calculating this depth yields for higher energies a depth of $\sim 26X_0$. In front of the first active layer a piece of absorbing aluminium ($0.02X_0$) is placed, which acts as a charged particle detector. As discussed before the detector consist of 24 layers which would return a total depth of around $23.3X_0$. However between layer 21 and 22 a piece of tungsten alloy is placed with thickness $6.7X_0$. As a result the total depth of the detector becomes $28X_0$.

The MIMOSA23 chips are made up of sensitive areas and insensitive areas. The pixel matrix serves as an active area, which generates the signals if particles pass through the sensor. The discriminators and control and output circuitry serve amongst other things for the data readout and processing. These insensitive areas don't give signals and therefore these insensitive areas are overlapped in one transverse direction to minimize for dead areas.

Figure 3.3: Schematic overview of the FoCal prototype.

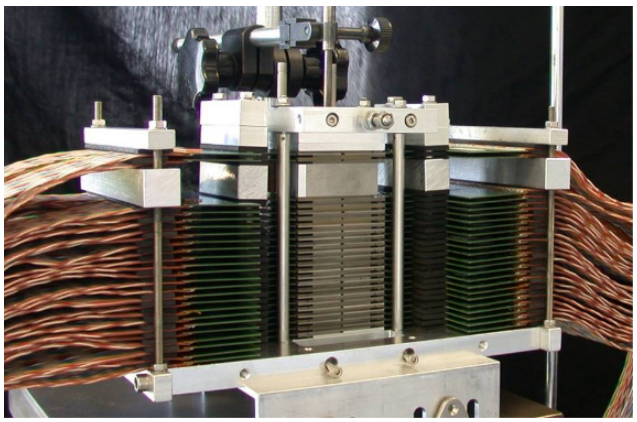

(a) Side view of the FoCal prototype [19]. Each layer consists of two modules which are installed in opposite direction. As can be seen this is beneficial for the cables which are connected to the PCBs.

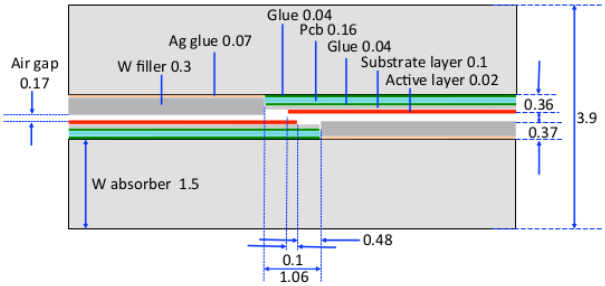

(b) A schematic overview of a layer in the x-z-direction [19]. As can be seen some gaps arise in the construction, which will have its consequences for the data analysis. Furthermore it can be seen that next to the module 0.3 mm of tungsten filler is placed.

One module is made up of two sensors which are attached to two printed circuit boards. Next to the sensor a tungsten filler plate of 0.3 mm is placed. One layer consists of two modules which are installed in opposite direction. Figure 3.3a shows a side view of the FoCal prototype. Installing the modules in the opposite direction is beneficial for the cables connected to the PCBs. Figure 3.3b shows the modules in the x-z-direction. Some gaps appear which are inevitable and have to be taken into account for the final data analysis.

3.4 Coordinate system

The detector consists of 24 layers, where the first layer is defined as $l = 0$. Each layer is defined into four quadrants (sensors). The four quadrants are numbered in a clockwise way. The coordinate system of the FoCal is presented in figure 3.4. The centre of the first layer ($l = 0$) is set to $(x, y) = (0, 0)$. Each chip can be divided in 640 lines and 640 columns. The column coordinate system is directed from the top to the bottom of a layer, i.e. the top of a chip in quadrant Q0 or Q3 has column number 0 and the bottom of a chip in quadrant Q1 or Q2 has column number 640. The line coordinated system is directed from the middle of the layer to the left and right, i.e. the left side of a chip in quadrant Q2 or Q3 has line number -320 and the right side of a chip in quadrant Q0 or Q1 has line number 230.

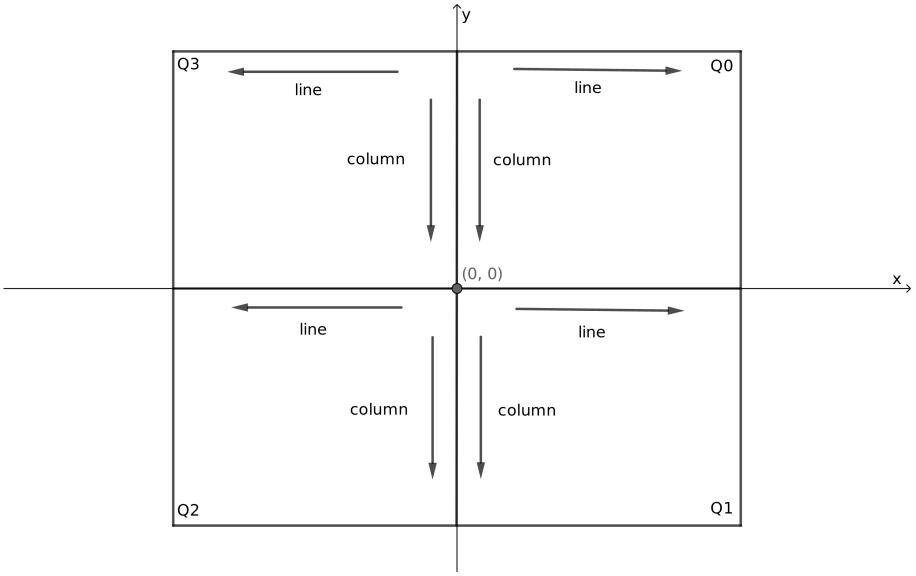

Figure 3.4: Schematic overview of the coordinate system used in the FoCal prototype. The quadrants (sensors) are numbered clockwise and the centre of the first layer ($l = 0$) is set to $(0, 0)$.

3.5 Trigger system

For the selection of events which yield the desired data, five trigger scintillators are installed as can be seen in figure 3.5. The trigger system has to start the data readout process when certain conditions are satisfied. Four of these trigger scintillators are placed in front of the first layer, one is placed behind the detector.

The P scintillator placed in front serves as a general trigger for incoming beam particles. When the P scintillator is triggered, it provides a gating signal for the other trigger scintillators in the system. The H and V trigger scintillator serve as a central trigger. The H scintillator is placed with its long axis in the x-direction, while the V scintillator is placed with its long axis in the y-direction. The overlapping part of the two covers an area of 10mm x 10mm. The F scintillator serves as an indicator for particles entering the front of the detector and the B scintillator as indicator for particles leaving the detector.

For electromagnetic showers the total shower energy should be contained inside the detector. Only electromagnetic showers with very high energy might possibly leave the detector and be indicated by the B scintillator. Furthermore, muons and hadronic shower leakage is indicated by the B scintillator. [5, 7, 18]

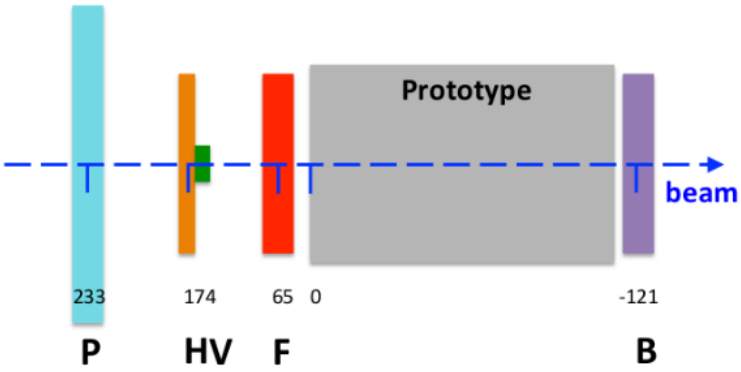

Figure 3.5: Schematic overview of the trigger system with its corresponding scintillators [18]. Four scintillators are placed in front of the detector, namely the P, H, V and F scintillator, which serve as trigger for incoming particles. The B scintillator serves as a indicator for showers/particles that totally traverse the detector.

3.6 Measurements

At DESY and at the CERN PS and SPS measurements with the prototype using test beams have been performed. The different types of beams and momenta used in the measurements are given in table 4:

Location	Year	Type of particle	Momentum p (GeV/c)	# of events
DESY T22	2014	e^+	2, 3, 4, 5.4	$9.5 \cdot 10^3$
CERN SPS H8	2014	e^-(mixed)	244	$1.6 \cdot 10^4$
CERN SPS H8	2014	e^+(mixed)	30, 50, 100	$3 \cdot 10^4$, $3 \cdot 10^4$, $8 \cdot 10^4$

Table 4: Overview of the measurements done with the FoCal prototype [19]. The measurements are performed with different particles with different momenta p. The mixture beams contain electrons/positrons and pions. The SPS data is of main interest for this thesis.

The data analysed in this thesis are taken from the SPS measurements at CERN, which means the particle beams with momenta of respectively 30, 50, 100 and 244 GeV/c.

4 Calibration procedure

The FoCal prototype is made up of 24 layers with four sensors in each layer as is discussed in section 3. In the prototype three different types of MIMOSA23 sensors are used. The differences between these sensors arise in the resistivity and thickness of the epitaxial layer as can be seen in table 3. Therefore the output signals might vary for the different sensors. Furthermore, sensors of the same type may also show differences in sensitivity. Clearly, this will have its consequences on the raw data and the following data analysis.

The active volumes of the sensors consist of a pixel matrix with dimensions 640 x 640. Some or more of the pixels might not work well and might have one of the following conditions:

- dead : the pixel is not working at all.
- hot : the pixel is oversensitive and returns too much noise.
- unstable : the pixel output differs over different runs.

The output of these bad working pixels is masked, since the data extracted from these pixels is not reliable. The masking process for the data runs used in this thesis is described in [22]. Besides these bad working pixels, the FoCal construction is such that dead and overlapping areas arise as is discussed in section 3.3. Particles passing through these dead areas will not be observed by a sensor and therefore no data for these particles can be extracted. The overlapping areas might return two signals for the same particle, so these overlapping areas are located and taken into account in the calculation of the lateral hit densities.

In the analysis of the data all these imperfections have to be taken into account. The data therefore has to be corrected by a calibration procedure, which will be discussed in this section. The calibration procedure makes use of the lateral hit densities to equalize the response of the chips and is based on the following assumptions [18]:

- The shower development of an electromagnetic shower is a symmetrical process around the shower axis (x_s, y_s).
- The sensitivity of the pixels inside a chip is uniform.
- After an inclination correction the particle beam impact is orthogonal to the layer plane for all layers.

4.1 Research objective

The data output of the FoCal prototype from SPS has been processed and afterwards masks have been created with the use of pedestal runs in [22]. The next step in the analysis of the FoCal prototype data is to correct for the sensitivity differences of the chips and for the large dead areas arising in the detector, which will be established by applying a calibration procedure. A calibration procedure for the FoCal prototype has been applied before to the SPS data in [18]. The research will focus on understanding existing C++ code written for the FoCal prototype, making the code work and trying to find improvements not only in the

code but also in the calibration procedure itself. The central question in this thesis therefore becomes: Is the calibration procedure applied before in [18] still a valid method to calibrate the processed data and/or do possibilities to improve the existing procedure and code exist?

4.2 Lateral hit densities

When a particle enters the detector, it will generate a shower of secondary particles. The showering process will continue until the shower particles are not energetic enough to produce more particles and eventually will be absorbed by the detector material. Since the shower produces initially more particles, in the beginning of the detector the number of hits increases in the longitudinal direction. This increase in particles will continue until the shower maximum is reached, after which the number of particles will decrease. Therefore in the layers before the shower maximum the hit density has to increase after which it will decrease until all particles are absorbed and the hit density is back to the noise level.

In the lateral direction, the number of hits is expected to be at its highest around the shower axis (x_s, y_s). As the Molière radius indicates, 90% of the shower energy should be contained within a cylindar of radius R_M. Therefore the energy deposited in the lateral direction has to decrease rapidly as the distance to the shower axis r increases. Since the number of hits is an indication of the energy, the number of hits will also decrease with r.

The applied mask screens the bad or not working pixels. The masked pixels will in this way be left out of the data analysis completely. When analysing the data, fully or partially masked sensors will have their affects on the analysis, because in these regions no information about the shower is known. This problem is solved by calculating the lateral hit density in the working regions and extrapolating the hit density for the masked zones. Since large parts of the chip surface might be masked during the masking process, the extrapolation is of utmost importance.

The lateral hit density is calculated as a function of the distance to the shower axis. The shower position can be determined from layer 0, which will yield an accurate position since the particle will only generate a single cluster. However, the shower has not started yet and a single cluster excites just a few pixels. Noisy pixels in the first layer could lead to a misidentification of the impact position of the incoming particle. The probability of that happening is decreased by applying a shower position finding procedure. The shower position is determined as follows [18, 19]:

- The centre of gravity in layer 3 and 4 gives a first approximation to the shower position:

$$(x, y)_{3,4} = \frac{1}{N} \sum_{i}^{N} (x_i, y_i), \tag{4.1}$$

  where N are the number of hits.

- Since further away from the shower axis the hit density decreases and the noise contribution increases, the calculation is repeated with a searching radius r around the

shower axis of 1 mm, which results in an accuracy improvement with respect to the step performed before.

- Combine the centres of gravity from layers 3 and 4:

$$(x,y)_{3,4} = \frac{1}{2}(\frac{1}{N_1}\sum_{i}^{N_1}(x_i,y_i) + \frac{1}{N_2}\sum_{j}^{N_2}(x_j,y_j)), \tag{4.2}$$

  where N_1 and N_2 respectively are the number of hits counted in layers 3 and 4 in step 2.

- The shower position/axis (x_s, y_s) is now calculated by searching for clusters in layer 0 around the shower position calculated in the previous step within a ring of radius $r = 1$ mm.

The distance r to the shower axis (x_s, y_s) is given by:

$$r = \sqrt{(x-x_s)^2 + (y-y_s)^2}. \tag{4.3}$$

The layer of interest for the calculation of the hit density is divided in rings of width Δr with radius r. The radius of the ring increments by 0.1 mm for $r < 2$ mm and increments by 0.5 mm for $r > 2$ mm. The width of the ring is thus defined as :

$$\Delta r = \begin{cases} 0.1\,\text{mm}, \text{ for } r < 2\,\text{mm} \\ 0.5\,\text{mm}, \text{ for } r > 2\,\text{mm} \end{cases} \tag{4.4}$$

In each ring the number of hits is counted and is used to calculate the hit density. The lateral hit density for quadrant q, layer l and radius of the ring r is given by:

$$\nu_{l,q}(r) = \frac{1}{A_{pixel}} \frac{\Delta N^{l,q}_{hit}(r) - \Delta N^{l,q}_{noise}(r)}{\Delta N^{l,q}_{pixel}(r)}. \tag{4.5}$$

Here $\Delta N^{l,q}_{hit}(r)$ is the counted number of hits in a ring of radius r, $\Delta N^{l,q}_{noise}(r)$ the number of noise hits in the same ring, $\Delta N^{l,q}_{pixel}(r)$ is the number of working pixels in the ring and A_{pixel} is the pixel size[9]. The noise hits $\Delta N^{l,q}_{noise}$ are obtained by counting the number of hits in a ring of radius r, where the noise hit profiles are obtained from pedestal runs. A pedestal run is a run where no beam is pointed on the detector and the hits obtained in the active volumes in these pedestal runs are solely due to detector noise.

The errors in the lateral hit density are calculated by the standard error of the mean[10]:

$$\sigma\nu_{l,q}(r) = \sqrt{\frac{\sum_{i\in events}^{events}(\nu_{l,q,i}(r) - \bar{\nu}_{l,q}(r))^2}{n^2}}. \tag{4.6}$$

[9]The pixel size dimensions are $30\mu m$ x $30\mu m$. The pixel size A_{pixel} therefore becomes $9 \cdot 10^{-10}\text{m}^2$.

[10]This is the version of the standard error of the mean used by ROOT, which approximates the ubiquitous version of the standard error of the mean known from statistics books for large n:

$$\sigma\nu_{l,q}(r) = \sqrt{\frac{\sum_{i\in events}^{events}(\nu_{l,q,i}(r) - \bar{\nu}_{l,q}(r))^2}{(n-1)n}}$$

.

Here the sum is over all the events in a run where inside the sum $\nu_{l,q,i}(r)$ is the hit density in a ring of radius r of a single event and $\bar{\nu}_{l,q}(r)$ is the mean hit density in a ring of radius r for all the events. n indicates the total number of events. The lateral hit density is calculated for each individual event in the run. However for the calibration factors the average hit density $\langle\nu_{l,q}\rangle$ will be used.

As was discussed before the lateral hit density will be extrapolated to correct for masked or dead areas. The number of hits in quadrant q and layer l is obtained by integrating and therefore extrapolating the lateral hit density:

$$\begin{aligned} N_{l,q}(R, \langle\nu_{l,q}\rangle) &= \int_0^{2\pi}\int_0^R \langle\nu_{l,q}(r)\rangle r dr d\theta \\ &= \int_0^R 2\pi r \langle\nu_{l,q}(r)\rangle dr, \end{aligned} \tag{4.7}$$

where R is equal to 22 mm. Alert readers might notice the integration over the whole ring, while the indices imply the number of hits for quadrant q in layer l. An integration over the surface of the ring which is covered inside the quadrant would be more appropriate. However, it is computational difficult to find this area since each event has a different shower position (x_s, y_s). By integrating the average lateral hit density of quadrant q over the whole surface of the ring for each quadrant, the conditions for each quadrant are the same. Since for the calculation of the calibration factors only the quotient of the average number of hits in a layer for each quadrant (discussed below) and the number of hits in a quadrant q is of interest, it has minor consequences for the calibration factors. Furthermore, the average lateral hit density is used in equation 4.7. Assuming that the probability of finding the shower position (x_s, y_s) in quadrant q is equal for all the quadrants, the assumption that the shower position will lie in the middle of the four quadrants can be made.

An estimate of the number of hits in layer l using the information of the quadrants (raw longitudinal profile) can be obtained by integrating the raw lateral hit densities. An estimate of the raw lateral hit density in layer l is:

$$\nu_l^r(r) = \frac{1}{A_{pixel}} \frac{\sum_{q=0}^{3}(\Delta N_{hit}^{l,q}(r) - \Delta N_{noise}^{l,q}(r))}{\Delta N_{pixel}^{l}(r)}. \tag{4.8}$$

$\Delta N_{hit}^{l,q}(r), \Delta N_{noise}^{l,q}(r)$ and $\Delta N_{pixel}^{l}(r)$ are the respectively the number of hits, the number of noise hits and the number of working pixels in a ring of radius r to the shower axis (x_s, y_s) for quadrant q in layer l. Integrating equation 4.8 over the surface of the rings from $R = 0$ mm to $R = 22$ mm, yields the estimated number of hits in layer l using the information of the quadrants:

$$\begin{aligned} N_l^r(R, \nu_{l,q}) &= \int_0^{2\pi}\int_0^R \nu_l^r(r) r dr d\theta \\ &= \int_0^R 2\pi r \nu_l^r(r) dr. \end{aligned} \tag{4.9}$$

The average number of hits per quadrant in a certain layer l is obtained by adding the number of hits in each quadrant and divide by the number of sensors in that layer. However, due to construction imperfections some of the 96 sensors do not work at all. Therefore the total number of hits after adding should not be divided by the number of sensors in that layer, but by the number of working sensors in that layer. The average number of hits per quadrant in layer l is given by:

$$N_l(R, \langle \nu_{l,q} \rangle) = \frac{1}{W_l} \sum_{q \in C_{l,q}}^{W_l} N_{l,q}(R, \langle \nu_{l,q} \rangle). \tag{4.10}$$

Here W_l is the number of working chips in layer l, $C_{l,q}$ is a list of working chips for each layer l quadrant q. $N_{l,q}(R, \langle \nu_{l,q} \rangle)$ is calculated as in equation 4.7. The procedure to attain W_l and $C_{l,q}$ is discussed in the next section.

4.3 Dead chips

Badly working or even dead pixels are excluded from the data analysis by the mask as was discussed in the introduction of this section. The mask structure is such that it is made up of a three dimensional histogram where a masked pixel has the value of '1' and a working pixel has the value of '0'. The two dimensional dimensions of the histogram are the same as the dimensions of the pixel matrix, which results in a total of 409600 pixels.

By reading out the mask and counting the number of ones in each chip, dead chips can be found and W_l nad $C_{l,q}$ can be constructed. This is done by setting a threshold on the number of ones. When the counted number of ones lies above the threshold value, the chip will be labeled as dead. The chip will not be taken into account in equation 4.10.

The threshold value has to be chosen near 409600 due to the fact that deviations from the mask might appear if the threshold is chosen lower. In such a case the chip will be labeled as dead but the chip still works partially and will therefore return a number of hits. Therefore a calibration factor for this chip is of interest and it has to be used in the analysis.

4.4 Calibration factors

The calculation of the calibration factors is the last step in the calibration procedure. The calibration factors have to correct for the different sensitivities of the chips used in the prototype and the dead areas arising from the construction.

At first the average number of hits per quadrant in each layer will be taken into account for each layer (equation 4.10) and a longitudinal profile as a function of the real shower is made. A gamma distribution of equation 2.10 is fitted through the raw data (averaged, equation 4.10) and parameters N, a and b are obtained. The calibration factors are obtained as the ratio of the fit values N_l^{fit} to the raw data per sensor:

$$c_{l,q} = \frac{N_l^{fit}}{N_{l,q}(R, \langle \nu_{l,q} \rangle)}. \tag{4.11}$$

Here $N_{l,q}(R, \langle \nu_{l,q} \rangle)$ gives the raw number of hits in quadrant q and layer l as defined in equation 4.7 and N_l^{fit} are the fit values at the real depth of the shower in units of X_0. Since every layer has four chips, a total of 96 calibration factors can be found. However, dead chips are not taken into account in the calibration procedure, so the calibration factor is previously set to 1 and the number of calibration factors attained in the procedure lies below 96. The calibration factors should be constant for different energies and the mean of the calibration factors should lie around 1.

4.5 Calibration of the raw data

The calibration procedure has been done and applying the calibration factors to the raw data equalizes the sensitivities of the chips. Applying the calibration factors results in the calibrated data which will be used to make longitudinal shower profiles.

The calibrated lateral hit density per layer is defined as:

$$\nu_l^c(r) = \frac{1}{A_{pixel}} \frac{\sum_{q=0}^{3} c_{l,q} \cdot (\Delta N_{hit}^{l,q}(r) - \Delta N_{noise}^{l,q}(r))}{\Delta N_{pixel}^{l}(r)}, \tag{4.12}$$

where $\Delta N_{hit}^{l,q}(r), \Delta N_{noise}^{l,q}(r)$ and $\Delta N_{pixel}^{l}(r)$ are the respectively the number of hits, the number of noise hits and the number of working pixels in a ring of radius r to the shower axis (x_s, y_s) for quadrant q in layer l. A_{pixel} is the pixel area and $c_{l,q}$ the calibration factor of the corresponding chip of quadrant q in layer l. The calibration has to equalize the response inside the quadrants of a certain layer. It is therefore expected that the calibration corrects the calibrated lateral hit density such that the lateral hit densities equalize.

The calibrated number of hits in each layer l can now be obtained by integrating the calibrated hit densities over the surface of the ring where the integration is from $R = 0$ mm to $R = 22$ mm:

$$\begin{aligned} N_l^c(R, \nu_{l,q}) &= \int_0^{2\pi} \int_0^R \nu_l^c(r) r dr d\theta \\ &= \int_0^R 2\pi r \nu_l^c(r) dr. \end{aligned} \tag{4.13}$$

The hits obtained from 4.13 are used to make longitudinal profiles. It is expected that this longitudinal profile follows a gamma distribution. The gamma distribution fit through this longitudinal profile will be of interest since according to the theory the parameters values have the comply with the following relations for the energy: $N \propto E$, $\alpha \propto \log(E)$ and $b =$ constant. The parameter values are also of interest for the calculation of the shower maximum using equation 2.11 and can be compared with the theoretical shower maximum obtained from 2.12. The theoretical shower maxima for the energies used in this thesis are presented in table 5, where a critical energy E_c of 8.1074 MeV is used, which is the critical energy of tungsten (W).

E (GeV)	30	50	100	244
t_{max} (X_0)	7.7	8.2	8.9	9.8

Table 5: The table presents the theoretical depth of the shower maximum (X_0) calculated with equation 2.11 for beams of respectively an energy of 30, 50, 100 and 244 GeV. The critical energy E_c used is 8.1074 MeV, which is the critical energy of tungsten (W).

At last it is of interest to check the differences in the RMS of uncalibrated and calibrated lateral hit densities. It is expected that the RMS will decrease for calibrated data. The calibration will correct for the different sensitivities between the chips inside the detector. Due to the correction, the spread in the lateral hit densities will decrease and therefore the RMS is expected to decrease for the calibrated lateral hit densities.
The data analysis and results of the calibration procedure will be discussed in the next section.

4.6 Software

The FoCal prototype data is analysed with ROOT [23], which is a program originally developed for particle physics data analysis by CERN. ROOT is an object-oriented program which is based on C++. The calibration procedure described before has been coded in C++ using text editor GNU Emacs. All the data output and figures resulting from the calibration procedure are generated with ROOT.

5 Calibration procedure results and analysis

The calibration procedure described in section 4 has been implemented in C++ and the results obtained by running the code in ROOT will be presented in this section. The syntax for the data analysis written in C++ and important functions of the code are discussed in appendix E.

In the analysis a total of four different beam energies is taken into account which respectively have an energy of $30, 50, 100$ and 244 GeV. In this section the calibration procedure results are discussed. For the sake of reducing the number of figures in this section the 100 GeV beam energy will be shown and the figures for the other energies will be placed in appendices which will be mentioned appropriately throughout this section.

5.1 Raw lateral hit densities

The raw lateral hit distributions are obtained by counting the number of hits in a ring of radius r and dividing by the number of working pixels in that ring for each event. The hit densities can be sorted in two groups: hit densities with noise and hit densities without noise. Since the objective of this thesis is to reproduce the calibration procedure and use the obtained calibration factors to generate longitudinal profiles, the hit densities without noise will be used throughout this section, i.e. equation 4.5 will be used.

The average raw hit density $\langle \nu_{l,q} \rangle$ is used for the raw lateral hit densities throughout the calibration procedure. The average raw lateral hit density as a function of the distance r to the shower axis in quadrant 0 is shown in figure 5.1 for the layers 3, 5, 7 and 9. The data is presented for a 100 GeV beam. The hit densities for the other three energies are presented in appendix B in figure B.1.

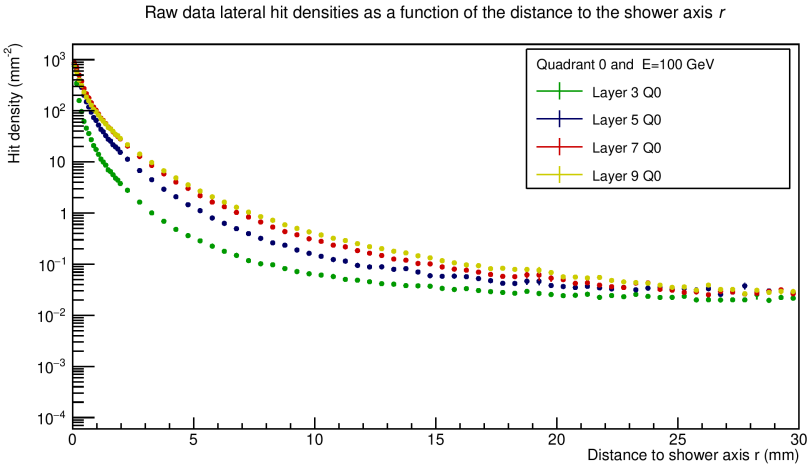

Figure 5.1: The average lateral hit densities obtained from raw data of 100 GeV electrons is presented as a function of the distance to the shower axis r. The densities are generated with data of quadrant 0 applied to equation 4.5 for four different layers: 3, 5, 7 and 9.

Figure 5.1 shows that the raw lateral hit density is at its highest close to the shower axis. The raw lateral hit density decreases rapidly for increasing r as expected. In the shower core the hit density shows fluctuations for different layers l, however when moving away from the shower core the lateral hit density increases for increasing layer number for layers before the shower maximum. Table 5 shows that the predicted shower maximum lies near layer 9 for a 100 GeV beam, so until the shower maximum is reached more particles will be produced, resulting in a higher hit density as can be seen from the figure.

Figure 5.2 shows the raw lateral hit densities in quadrant 0 as a function of the distance r to the shower axis for the layers 11, 13, 15 and 17. In the shower core the lateral hit density shows again fluctuations. When looking at the figure it can be seen that when moving away from the shower core the hit density decreases for increasing layer l. After the shower maximum the number of particles decreases and eventually will be absorbed by the material of the detector. The figure shows the hit densities after shower maximum and is therefore in line with the expected theory. The figures for the other energies are shown in figures B.2.

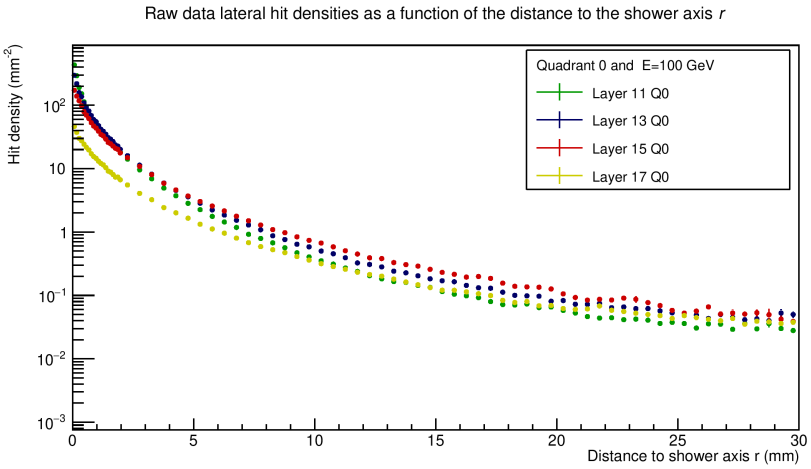

Figure 5.2: The average lateral hit densities obtained from raw data of 100 GeV electrons is shown as a function of the distance to the shower axis r. The densities are generated with data of quadrant 0 applied to equation 4.5 for four different layers: 11, 13, 15 and 17.

5.2 Raw longitudinal hit profiles

The raw longitudinal hit profiles are obtained by integrating the averaged raw lateral hit density profiles over the full surface of the ring of radius r for each r. The integration corrects for the dead or masked areas. The results of the integration of the lateral hit densities for the four quadrants are shown in figure 5.3 for a beam of $E = 100$ GeV. Figures B.3, B.4 and B.5 show the longitudinal hit profiles for the other energies.

From figure 5.3 can be obtained that the longitudinal profile has an erratic pattern. The erratic shape of the longitudinal profiles is caused by the differences in chip sensitivities and the appearance of dead chips in the detector. Some of the layers in a certain quadrant (for

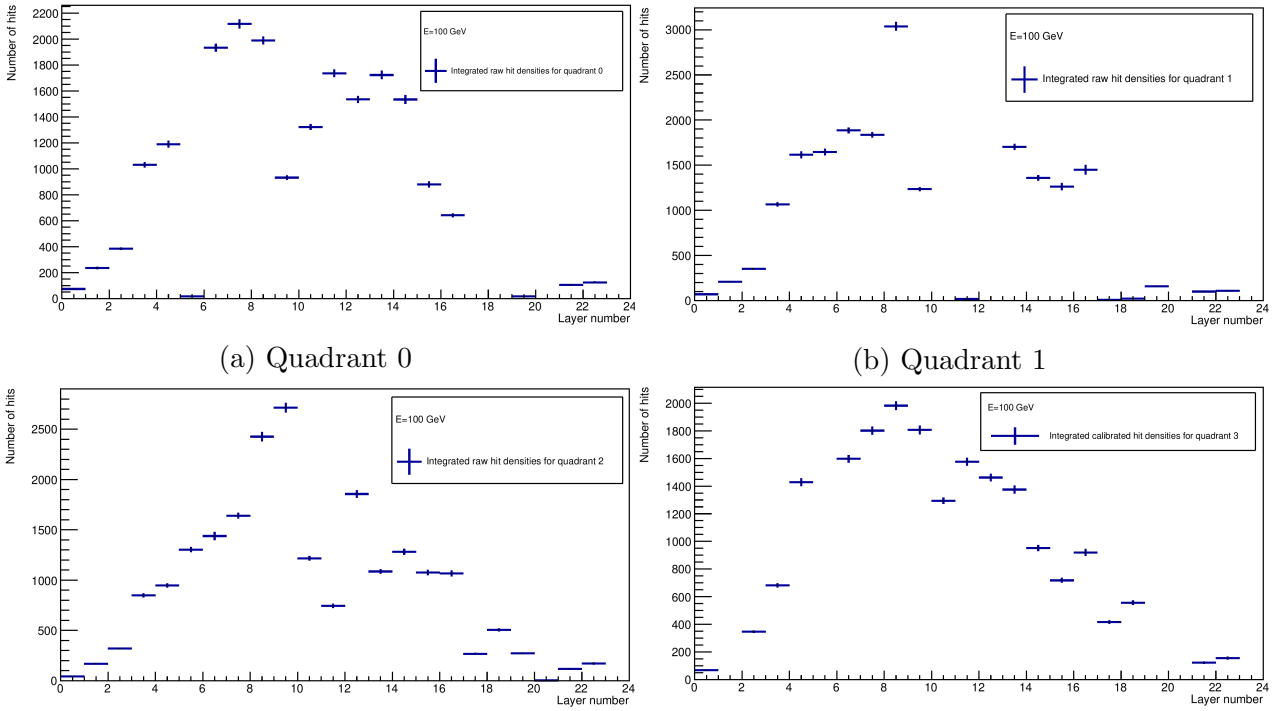

(a) Quadrant 0

(b) Quadrant 1

(c) Quadrant 2

(d) Quadrant 3

Figure 5.3: The raw longitudinal hit profiles for each quadrant attained by integrating the raw lateral hit densities as function of the layer number. The profiles are shown for a beam energy of a 100 GeV.

example layer 21 quadrant 0) do not return a number of hits or if they do the number of hits is very low with respect to surrounding layers. This might be explained by dead sensors and it is therefore of utmost importance to locate the positions of dead sensors inside the detector. An estimate of the number of hits in layer l using the information of the quadrants (raw longitudinal profile) for a beam of 100 GeV shows the same erratic pattern. The estimated hit profile (equation 4.8) for $E = 100$ GeV is shown in figure 5.4 as a function of the real layer depth with a gamma distribution fitted through to the data points.

5.3 Dead sensors

The dead sensors in the FoCal detector have a large influence on the data analysis and therefore also on the calibration procedure. To correct for these influences, the dead chips and their corresponding positions in the detector have to be taken into account.
As discussed in section 4 the MIMOSA23 sensor has a pixel matrix which is made up of 409600 pixels. The threshold on the number of masked pixels in the sensor is set to 406000, which means that if the number of working pixels is less than $\sim 0.9\%$, the sensor is labeled as dead. The sensors which are partially masked have enough data and statistics to apply a dead zone extrapolation. However for a sensor without data or very little data, the statistics are too low to apply the extrapolation. Figure 5.5 shows the number of masked pixels per chip.

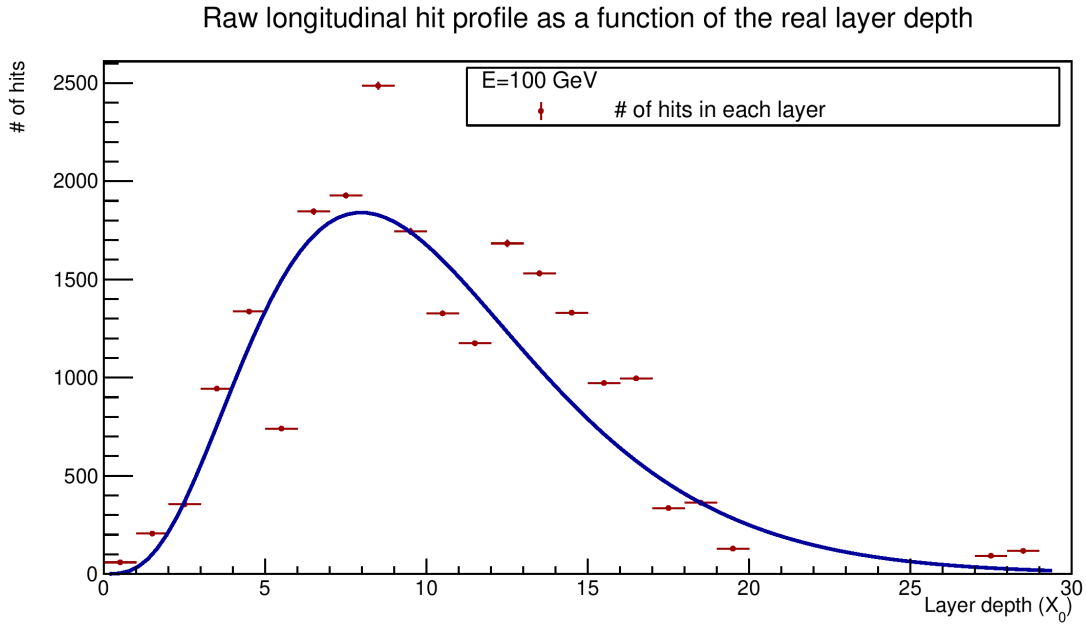

Figure 5.4: An estimate of the number of hits in layer l using the information of the quadrants (raw longitudinal profile, equation 4.8) shown as a function real depth of the layer in the stack in units of X_0. The data points are shown in red. The gamma distribution of 2.10 is fitted through the data points and indicated by the blue line. The beam energy used to obtain this profile is $E = 100$ GeV.

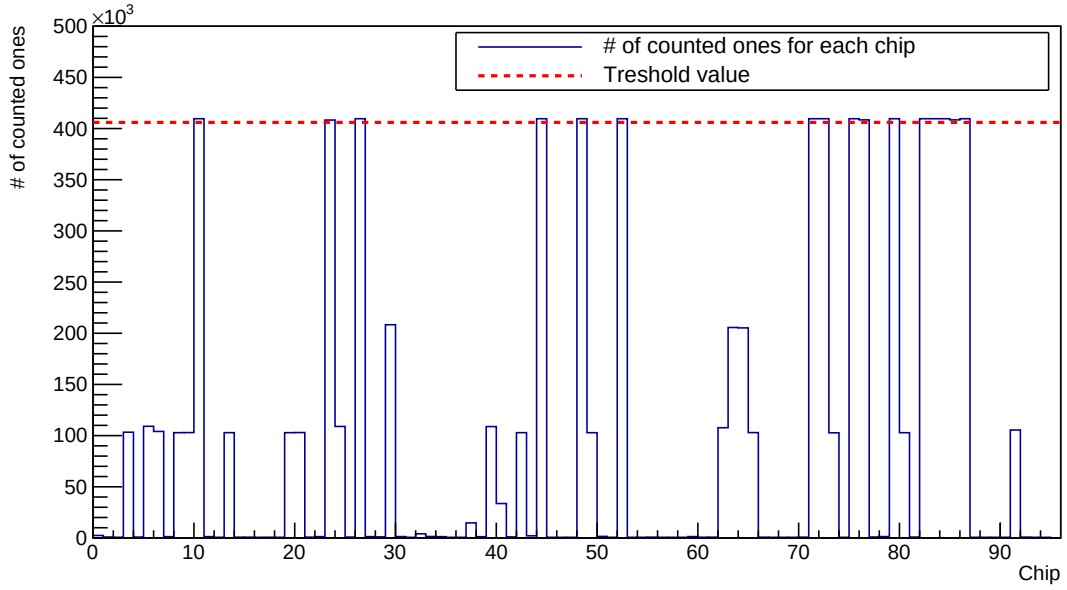

Figure 5.5: The number of masked pixels obtained from the mask for each chip in the detector (blue) together with the threshold value of 406000 masked pixels (red).

As can be seen from figure 5.5 16 chips have to be labeled as dead. These dead sensors

are listed by position in table 6, i.e. the layer in which the sensor appears with corresponding quadrant.

L	Q	L	Q	L	Q	L	Q
2	3	12	1	19	0	21	0
6	0	13	1	19	1	21	1
6	3	18	0	20	0	21	2
11	1	18	1	20	3	21	3

Table 6: The table lists the dead sensor inside the FoCal prototype. The dead sensors are indicated by their position in the prototype, i.e. the layer and quadrant where the dead sensor appears.

5.4 Averaging the hits in each layer

The calibration factors are found from a fit of the average number of hits per quadrant. In section 4 it is discussed that for the averaging of the number of hits in each layer, it is important to average the number of hits in a layer l obtained from working sensors. The number of working chips in each layer is listed in table 7

L	Working chips	L	Working chips	L	Working chips	L	Working chips
0	4	6	2	12	3	18	2
1	4	7	4	13	3	19	2
2	3	8	4	14	4	20	2
3	4	9	4	15	4	21	0
4	4	10	4	16	4	22	4
5	4	11	3	17	4	23	4

Table 7: The number of working chips in each layer of the FoCal prototype. The table is constructed from table 6.

With the help of table 7 the average number of hits in each layer obtained from the raw longitudinal profiles per quadrant (see figure 5.3) are found. The average data points are positioned at the real depth of the layers in the stack in units of X_0. Through this average hit profile the gamma distribution of equation 2.10 is fitted. The result for a 100 GeV beam is shown in figure 5.6.

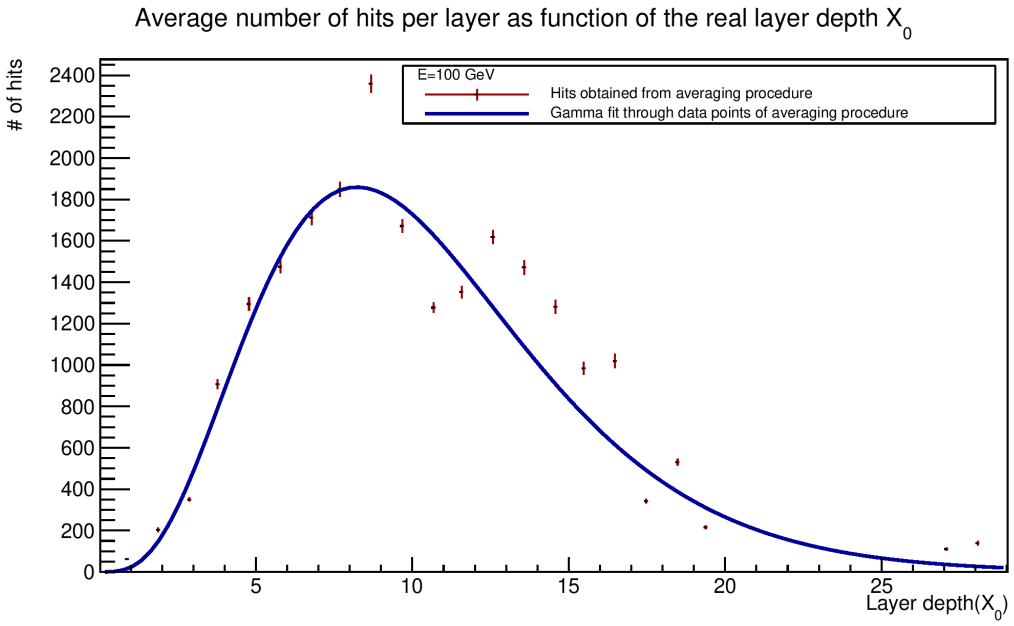

Figure 5.6: The average number of hits per quadrant for each layer (red points) which is found by adding the number of hits in each layer for all quadrants (5.3) and dividing it through the number of working chips in the layer. The gamma distribution of equation 2.10 is fitted through the data points (blue line). The average data points represent the number of hits at the real depth in the stack (X_0) of layer l. The beam energy of interest for these data is $E = 100$ GeV.

The gamma distribution is used to extract 24 data points which will be used for calculating the calibration factors. These 24 data points are found by filling in the real layer depth in X_0 in the obtained gamma distribution fit. The average hit profiles per quadrant for each layer made for the other energies are presented in B.6

5.5 Calibration factors

The calibration factors for each layer are calculated by dividing the fitted number of hits N_l^{fit} found at the real depth of the corresponding layer through the number of hits in each quadrant for the corresponding layer (equation 4.7). The result is 4 calibration factors for each layer, which gives a total of 96 calibration factors. The calibration factors of the dead quadrants (chips) are flagged and are set to a value of $'1'$. Since the fraction of the fitted number of hits with the number of hits in a certain quadrant is taken, there are values of the calibration factor that do not make any sense. Therefore a threshold of 40 is put on the calibration factors. If the calibration factor is higher than 40, the calibration factor for that quadrant is flagged and set to a value of $'1'$. The calibration factors are obtained for the four different energies and are shown in figure 5.7. Since for some regions the calibration factors shown in figure 5.7 are behind the factors for other energies, the calibration factors for each energy are plotted separately in figures B.8a, B.8b, B.8c and B.8d. The calibration factors should be energy independent. Looking at figure 5.7 it can be concluded that the

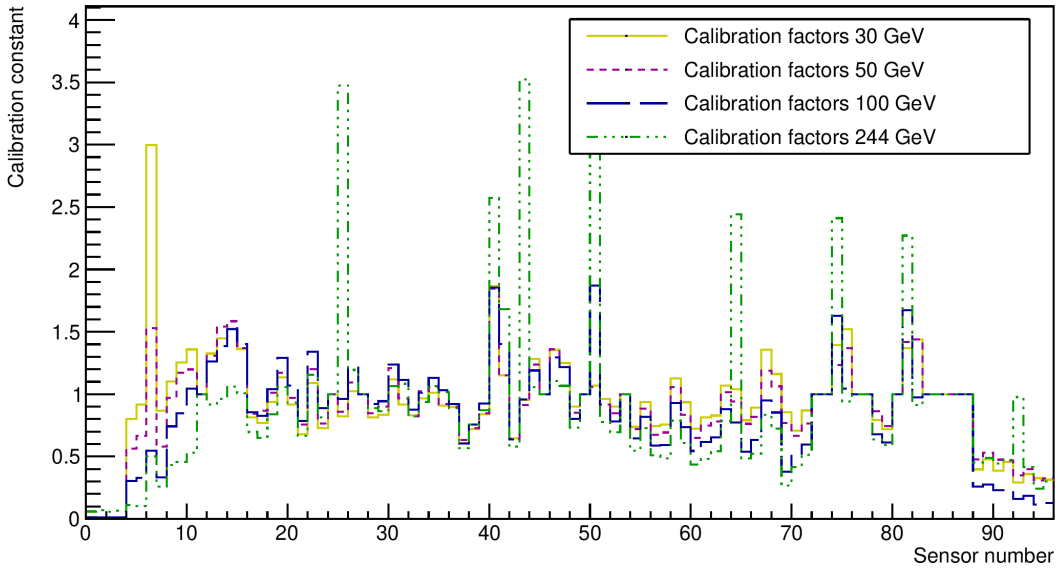

Figure 5.7: The calibration factors of the 96 chips used in the FoCal prototype for the four different SPS beam energies: 30, 50, 100 and 244 GeV.

calibration factors show very little energy dependence for most chips. However there appear some outliers in the calibration factors for 244 GeV.

5.6 Calibrate the raw data

The calibrated lateral hit densities per layer are calculated using equation 4.12. The calibrated lateral hit densities are shown for the layers 5, 9, 13 and 17 as a function of the distance r to the shower axis in figure 5.8. The energy used is $E = 100$ GeV.

The calibration has to equalize the response in the quadrants for a certain layer. The raw and calibrated lateral hit density profiles for layer 5 are shown in figure ... for each quadrant using an energy of 100 GeV.

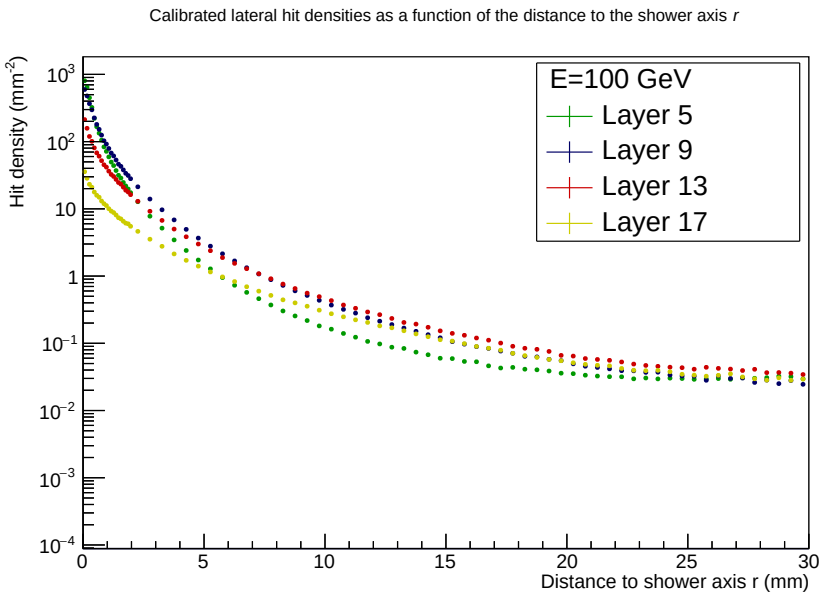

Figure 5.8: The calibrated lateral hit densities as a function of the distance r to the shower axis (x_s, y_s) for the layers 5, 9, 13 and 17. The calibrated hit densities are obtained from equation 4.12. A beam energy of 100 GeV is used.

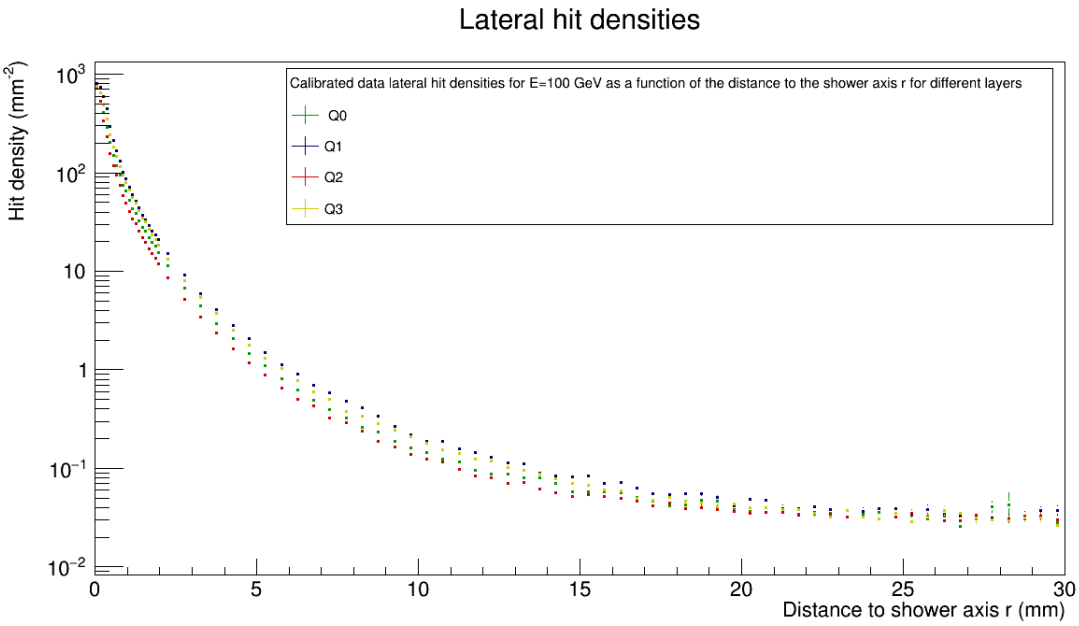

(a) Raw lateral hit densities

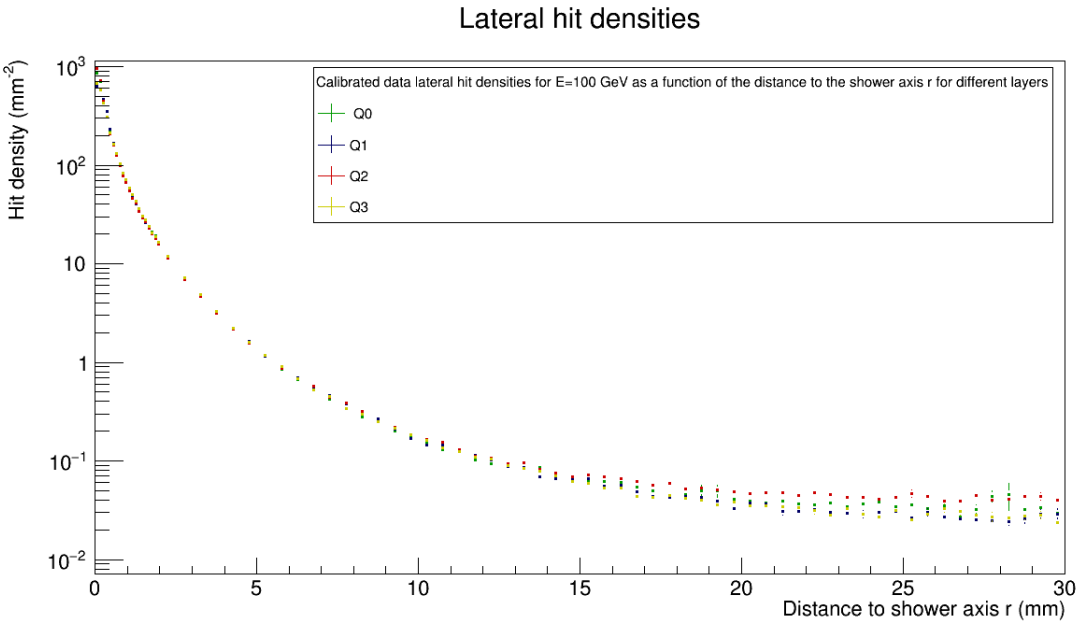

(b) Calibrated lateral hit densities

Figure 5.9: The lateral hit densities in layer 5 for a 100 GeV beam are shown as function of the distance to the shower axis r. The upper figure shows the raw lateral hit densities and the lower figure shows the calibrated lateral hit densities.

Figure 5.9 shows that after the calibration the lateral hit densities lie closer to each other than before the calibration. In the tail (i.e. far away from the shower axis) the separation between the different lateral hit densities becomes larger. However, since the lateral hit densities around the shower axis are of main importance, it can be concluded that the calibration equalizes the responses properly.

Integrating the calibrated hit densities over all r returns the calibrated longitudinal hit profiles. The calibrated hit profile for a beam of $E = 100$ GeV is shown in figure 5.10 and a gamma distribution is fitted through the data points. The calibrated longitudinal profiles for the other energies are shown in B.10.

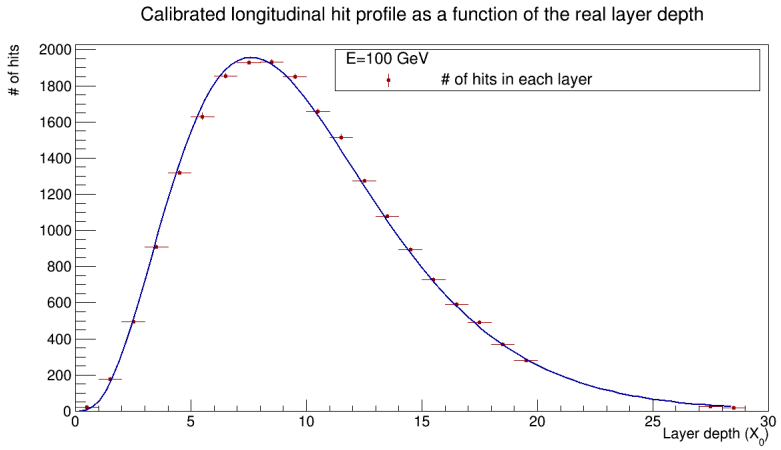

Figure 5.10: The longitudinal hit profile obtained by calibrating the raw data as function of the real layer depth in units of X_0 (red points). The gamma distribution of equation 2.10 is fitted through the longitudinal profile (blue line). The beam energy of interest is $E = 100$ GeV.

Figure 5.10 shows that most of the points are approximately gamma distributed. As discussed in section 4 the normalisation factor N of the gamma distribution fit should scale with energy, the factor a should scale with the logarithm of the energy and the factor b should be constant. The normalisation factor N, factor a and factor b as a function of the beam energy are shown in figure 5.11.

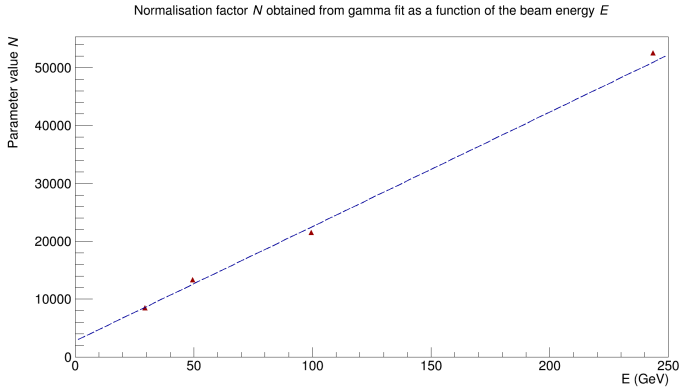

(a) The normalisation factor N (red triangles) obtained from the gamma distribution fit through the calibrated longitudinal profiles presented as function of the energy E. The blue dashed line indicates the expected relationship $N \propto E$.

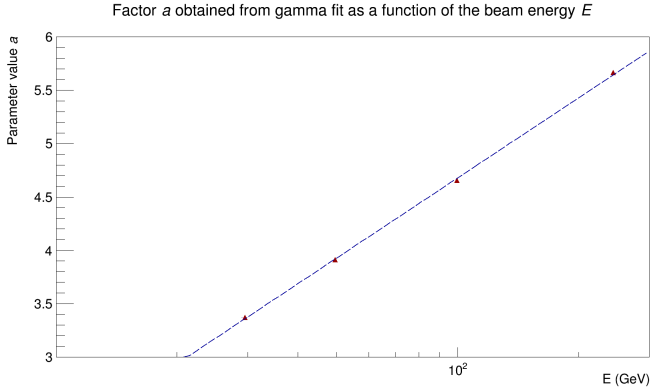

(b) The factor a (red triangles) obtained from the gamma distribution fit through the calibrated longitudinal profiles presented as a function of the energy E. Note that the x-axis is log-scaled. The blue dashed line indicates the expected relationship $a \propto log(E)$.

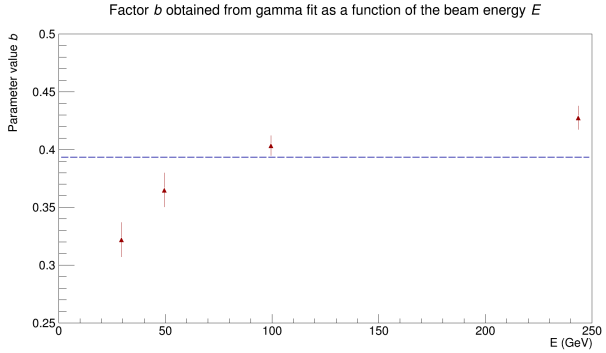

(c) The factor b (red triangles) obtained from the gamma distribution fit through the calibrated longitudinal profiles as a function of the energy E. The blue dashed line indicates the relationship $b = \text{constant}$

Figure 5.11: The parameter values of the gamma distribution fit through the calibrated longitudinal hit profiles as a function of the energy E. The parameter values are expected to follow relation which are indicated by the blue dashed lines.

If the data is inspected by eye, the normalisation factor N seems to scale with energy and the factor a seems to scale with the logarithm of the energy. However the factor b shows deviations from the expected behaviour for different energies. These deviations are on the other hand in the order of 10^{-1} and the errors in the values of b in the order of $\sim 0.01 - 0.025$.

With the help of the parameter values of the gamma distribution fit for the different energies, the position of the shower maximum can be calculated with equation 2.11. The parameter values for each energy and the corresponding shower maximum are listed in table 8.

E	30 GeV	50 GeV	100 GeV	244 GeV
N	$(8.5 \pm 0.030) \cdot 10^3$	$(13.4 \pm 0.046) \cdot 10^3$	$(21.6 \pm 0.051) \cdot 10^3$	$(52.7 \pm 0.14) \cdot 10^3$
a	3.37 ± 0.01	3.91 ± 0.02	4.66 ± 0.01	5.67 ± 0.02
b	0.34 ± 0.01	0.39 ± 0.01	0.45 ± 0.01	0.50 ± 0.01
$t_{max}(X_0)$	6.88 ± 0.01	7.54 ± 0.01	8.16 ± 0.01	9.34 ± 0.01

Table 8: The parameter values of the gamma distribution fit through the calibrated longitudinal profiles with corresponding errors. The corresponding shower maximum is calculated from equation 2.11 and listed below the parameter values.

It is expected that the RMS of the lateral hit densities decreases after the calibration. The RMS for uncalibrated and calibrated lateral hit densities in the same layer and quadrant is shown in figure 5.12 for a 100 GeV beam.

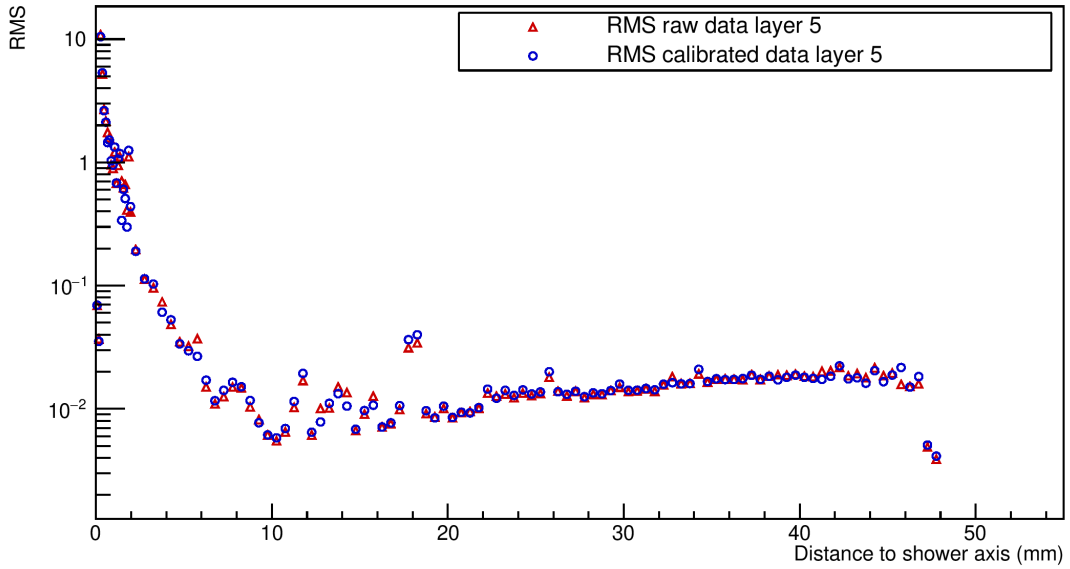

Figure 5.12: The root mean squared (RMS) for the calibrated and uncalibrated raw lateral hit densities plotted as a function of the distance to the shower axis r. The raw data RMS data points are indicated by red triangles and the calibrated RMS data points are indicated by blue circles.

Figure 5.12 shows that the RMS decreases after the calibration. However, since the differences are small and difficult to observe, the RMS will be divided by the mean for each r, which will be called RMS-standardized. The ratio of the RMS-standardized after calibration to the RMS-standardized before calibration is calculated for each r with corresponding errors and is shown in figure 5.13.

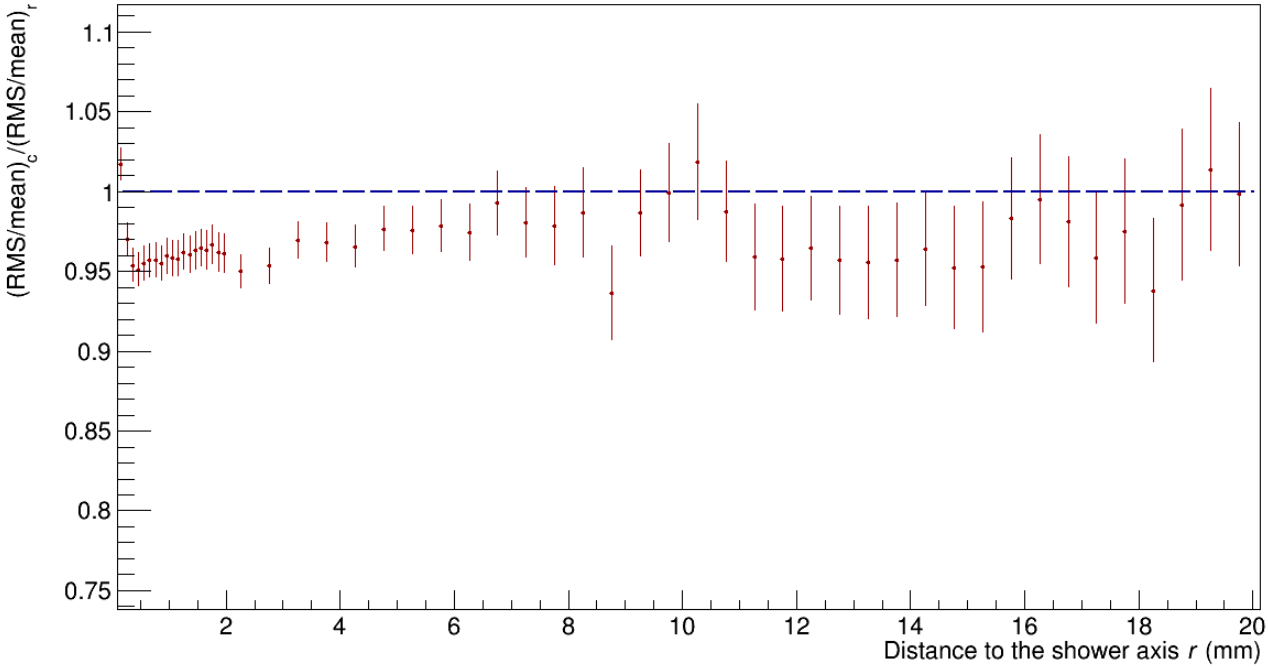

Figure 5.13: The ratio of the $\frac{RMS}{mean}$ of the calibrated lateral hit densities to the $\frac{RMS}{mean}$ of the raw lateral hit densities (red points) as a function of the distance to the shower axis r. The blue dashed line indicates the value of 1.

Figure 5.13 shows that for most r the ratio of the RMS-standardized after calibration to RMS-standardized before calibration lies below 1. This result is expected since the calibration corrects for the sensitivities of the chips, which leads to a smaller spread in the data points and therefore a smaller RMS. However the point closest to the shower axis is interestingly since it lies above 1. The deviations close to the shower axis of the lateral hit densities might be a reason for this anomaly. The ratio lies for almost the whole range of figure 5.13 below 1, which implies that the calibration works well and improves the RMS-standardized ratio. Figure 5.12 shows that the RMS for calibrated data is lower than for uncalibrated data. The calibration corrects for the sensitivities of the chips, which leads to a smaller spread in the data points and therefore a smaller RMS.

6 Conclusion

The data processed and masked in [22] has been calibrated for the four energies 30, 50, 100 and 244 GeV following the procedure discussed in section 4. The FoCal prototype is a high granularity calorimeter, which results in a high number of hits and implicitly a high hit density close to the shower axis (x_s, y_s). The hit density decreases rapidly for increasing distance r from the shower axis which is shown in section 5. Due to the small Molière radius (R_M) of the detector this is the expected result since 90% of the shower energy has to be contained within a radius of R_M. This result holds for the raw and calibrated lateral hit densities.

For the calculation of the calibration factors the raw longitudinal hit profiles are of interest. The raw longitudinal hit profiles showed an erratic pattern which is induced by the sensitivity differences in the chips and the appearance of dead sensors in the detector. The values obtained from the gamma distribution fit through the hit profile which is made up of the average of the hits in the four quadrants has been improved. By taking the average of the hits in the four quadrants, the appearance of bad sensors has been ignored. The sum of the hits in the four quadrants divided by the total number of chips in a layer where dead chips appear, will push the fit through the average hit profile down since a dead chip does not return hits. To solve this problem the dead sensors in the prototype have been located and only hits in working quadrants are taking into account for the averaging procedure.
The resulting data points will give a better representation of the real detector and the gamma distribution fit will not be affected by the low number of hits in layers where for example only half of the chips works. The 'new' method has been implemented in the calibration procedure which results in more accurate calibration factors, which should as a consequence in principle better apply to the FoCal prototype. The calibration factors look more or less energy independent, however the 244 GeV calibration factors show some outliers.

The calibration factors are applied to the raw lateral hit density distributions to obtain longitudinal hit profiles. The calibration has its desired effect on the longitudinal hit profiles. The longitudinal hit profiles have lost their erratic pattern and the data points follow a gamma distribution. Fitting a gamma curve through the longitudinal hit profile returns the fit values N, a and b of equation 2.10. The normalisation factor N seems by eye to be linear in the energy E, which is the expected relation. The factor a seems by eye to scale with the logarithm of the energy E, which is also expected. Looking at the factor b, it seems not to be constant. However the deviations in the parameter values of b are relatively small.

The depth of the shower maximum deviates by $0.5 - 0.9\ X_0$ from the theoretical calculated shower maximum, which is in the order of tens of percents. The shower maximum is structurally shifted to the left, which might be caused by the physics inside the detector.
The RMS is improved by applying the calibration procedure to the raw data, i.e. the RMS is smaller after calibration. The RMS measures the spread in individual data points. The calibration procedure corrects the differences in sensitivities for each chip. The spread in the data points at each distance r to the shower axis will become smaller and the RMS therefore too. Furthermore, the ratio of the RMS-standardized lies for most of the distances to the shower axis r below 1, so the calibration procedure significantly improves the RMS.

The calibration procedure has been carried out and its validity has been proven. One of the steps in the calibration procedure has been improved and the improvement is implemented in this thesis. Large improvements have been made in the C++ code itself. The C++ code of the calibration procedure is more user friendly now and some of the methods have been partially or totally rewritten.

7 Discussion

The validity of the calibration procedure has been proven, however in some of the steps carried out appear some anomalies or possibilities to make the procedure more accurate. Furthermore the procedure has been tested on other aspects, think of position of the shower maximum, parameter values of the gamma distribution fits or the RMS of the lateral hit densities.

The lateral hit densities (uncalibrated and calibrated) depend on the difference between the counted number of hits and the number of counted noise hits in a ring of radius r. Pedestal runs have been analysed to obtain the number of noise hits in a run. The noise used in the calculations for the lateral hit densities uses the average noise (number of counted hits in a pedestal) obtained from the pedestal. However, since noise is a stochastic process and therefore differs for each event, it will be better to subtract the noise where each pixel is assigned with a probability of being a noise pixel. Another way to improve the subtraction of the noise will be to assign a label which depends on the time to each pedestal. When calculating the lateral hit densities for each run, the pedestal belonging to that run will be used in the calculation. Since noise can also be dependent on the position of the chip, it will be better to use the pedestal instead of assigning a possibility of being a noise pixel to each pixel.

The raw longitudinal hit profile for a quadrant q is obtained by integrating the average raw lateral hit densities over the whole surface of the ring with width Δr and radius r. However, the lateral hit density is different for each quadrant. To correctly calculate the number of hits obtained from a raw lateral hit distribution in quadrant q, the integration should be over the area of the ring covered in quadrant q. The area of the ring covered in a certain quadrant q depends on the location of the shower axis (x_s, y_s). The location of the shower axis differs for each event, which results in a lot of additional code. However, to obtain more accurate lateral hit densities, and as a result better calibration factors, this method has to be carried out. To attain the area of the ring covered in a certain quadrant, a Monte-Carlo simulation can be implemented. In each quadrant a lot of points are uniformly distributed. By counting the points which satisfy the boundary conditions of the ring and the quadrant and dividing this number through the total number of distributed points, the area of the area can be estimated. The estimation can be improved by distributing more points. Since the area of the ring for each event is required, it will cost a lot of computing power and a lot of time to apply this Monte-Carlo simulation.

Taking the calibration factors into consideration it follows directly that the 244 GeV data shows more outliers than the other energies. This might be explained by the fact that the measurements with the 30, 50 and 100 GeV beams have been performed at another moment than the measurements with the 244 GeV beam. As a result some settings of the chips might have been manually adjusted which results in a different sensitivity for a few sensors and therefore a different calibration factor. The mean value of the calibration of the calibration factors has to lie near 1. This seems to hold for the all the energies. However a note has to be made since the very high calibration factors are left out of the analysis and the sensors 1 up to 4 return a very low calibration factor, which is probably due to the shape of the gamma

curve in the first layers.

The fit values of gamma distribution fits for all the energies looked by eye to follow the desired relations. However, the errors in especially the data points of the normalization factor N and factor a are very small. Fitting the desired relationship through these data points will result in a very high χ^2 due to the low errors. Basing the conclusion for the relation to hold on statistical grounds, the relationship will not hold since the data is not consistent to the fit for values of $\chi^2 \gg 1$.

The SPS data has been analysed in this thesis and the calibration procedure proves its validity. However, to perform another test on the validity of the calibration procedure the DESY data might be analysed as well. This data is taken at another moment at another location so it will be interesting to see if the data follows the expected behaviour described in section 4.

References

[1] CERN, *The standard model*, URL https://home.cern/science/physics/standard-model.

[2] E. Wessels, Ph.D. thesis, VU Amsterdam (2009), URL https://www.nikhef.nl/pub/services/biblio/theses_pdf/thesis_E_Wessels.pdf.

[3] D. J. Griffiths, *Introduction to elementary particles; 2nd rev. version*, Physics textbook (Wiley, New York, NY, 2008), URL https://cds.cern.ch/record/111880.

[4] A. Khodjamirian, *Quantum chromodynamics and hadrons: an elementary introduction*, URL http://www.hep.shef.ac.uk/edaw/PHY206/Site/2012_course_files/phy206rlec7.pdf.

[5] M. Reicher, Ph.D. thesis, Utrecht University (2016), URL https://www.nikhef.nl/pub/services/biblio/theses_pdf/thesis_M_Reicher.pdf.

[6] A. Ranjan and V. Ravishankar, *Introduction to quark-gluon plasma*, URL https://link.springer.com/content/pdf/10.1007%2Fs12648-010-0007-1.pdf.

[7] H. Wang, Ph.D. thesis, Utrecht University (2017), URL https://www.nikhef.nl/pub/services/biblio/theses_pdf/thesis_H_Wang.pdf.

[8] R. Plačakytė, *Parton distribution functions*, URL https://arxiv.org/pdf/1111.5452.pdf.

[9] T. Peitzmann, *Parton Distribution Functions and Forward Physics at the LHC*, slides meeting FoCal group.

[10] The FoCal Collaboration, *Letter of Intent: A Forward Electromagnetic Calorimeter (FoCal) in the ALICE experiment*, URL https://indico.cern.ch/event/102718/contributions/14229/attachments/9309/13663/focal-loi-0-1.pdf.

[11] V. Kaushik, *Electromagnetic Showers and Shower Detectors*, URL http://www-hep.uta.edu/hep_notes/general/general_0001.pdf.

[12] C. Fabjan and F.Gianotti, Reviews of Modern Physics **75**, 1243 (2003), URL http://lappweb.in2p3.fr/~chefdevi/Detector_reports/Calorimetry/Fabjan.pdf.

[13] H. Bichsel and D.E. Groom and S.R. Klein, *33. Passage of Particles Through Matter (Revised August 2015)*, URL http://pdg.lbl.gov/2018/reviews/rpp2018-rev-passage-particles-matter.pdf.

[14] H. Oberlack, *Calorimetry in Particle Physics*, Lecture slides, URL https://indico.mpp.mpg.de/event/a0632/contribution/s0t52/material/0/0.pdf.

[15] R. Wigmans, *Calorimetry: Energy measurement in particle physics*, vol. 107 (Oxford University Press, 2000).

[16] Erika Garutti, *The physics of particle detectors*, Lecture notes, URL http://www.desy.de/~garutti/LECTURES/ParticleDetectorSS12/L2_Interaction_radiationMatter.pdf.

[17] M. Berger and S. Seltzer, *Studies in penetration of charged particles in matter* (1964).

[18] C. Zhang, Ph.D. thesis, Utrecht University (2017), URL https://www.nikhef.nl/pub/services/biblio/theses_pdf/thesis_C_Zhang.pdf.

[19] A. de Haas et al., *The FoCal prototype - an extremely fine-grained electromagnetic calorimeter using CMOS pixel sensors*, URL https://iopscience.iop.org/article/10.1088/1748-0221/13/01/P01014/pdf.

[20] *Particle Data Group*, URL http://pdg.lbl.gov/2019/2019/AtomicNuclearProperties/index.html.

[21] A. Himmi et al., *PHASE-1: User Manual*, Institut de Recherches Subatomiques IN2P3-CNRS / ULP Strasbourg France (2008), URL http://www.iphc.cnrs.fr/IMG/PH1-UserMan-20080916.pdf.

[22] M. Waterlaat, *FoCal: Data Analysis on an extremely fine grained digital calorimeter*.

[23] *ROOT- Data Analysis Framework*, URL https://root.cern.ch/.

[24] M. van Leeuwen, *Quark cluster instructions*, URL http://www.staff.science.uu.nl/~leeuw179/bachelor_research/quark_cluster.html.

A Pseudorapidity

In this subsection the derivation of the pseudorapidity η is given, which is based on the theory in [4]. The pseudorapidity will be derived from the definition of the rapidity y. Algebraic steps will not be discussed in detail. The definition of the rapidity is given by:

$$\begin{aligned} y &= \frac{1}{2}\ln\frac{E+p_Lc}{E-p_Lc} \\ &= \frac{1}{2}\ln\frac{\sqrt{p^2c^2+m^2c^4}+p_Lc}{\sqrt{p^2c^2+m^2c^4}-p_Lc} \\ &= \frac{1}{2}\ln\frac{pc\sqrt{1+\frac{m^2c^4}{p^2c^2}}+p_Lc}{pc\sqrt{1+\frac{m^2c^4}{p^2c^2}}-p_Lc} \end{aligned} \tag{A.1}$$

Here in line two the energy for a particle with momentum p_L is substituted. The formula for this energy is given by:

$$E^2 = (pc)^2 + (mc^2)^2, \tag{A.2}$$

where mc^2 denotes the rest energy of the particle. Since highly relativistic particles are taken into account: $pc \gg mc^2$. Therefore the square root in the numerator and denominator can be Taylor expanded. The Taylor expansion for $(1+x)^{1/2}$ is given by:

$$\begin{aligned} (1+x)^{1/2} &= 1+\frac{1}{2}x+\mathcal{O}(x^2) \\ &\simeq 1+\frac{1}{2}x \end{aligned} \tag{A.3}$$

Now substituting this expression in the numerator and denominator with $x = \frac{m^2c^4}{p^2c^2}$, the following is obtained:

$$\begin{aligned} y &\simeq \frac{1}{2}\ln\frac{pc(1+\frac{m^2c^4}{2p^2c^2})+p_Lc}{pc(1+\frac{m^2c^4}{2p^2c^2})-p_Lc} \\ &\simeq \frac{1}{2}\ln\frac{pc+\frac{m^2c^4}{2pc}+p_Lc+...}{pc+\frac{m^2c^4}{2pc}-p_Lc+...} \\ &\simeq \frac{1}{2}\ln\frac{1+\frac{p_L}{p}+\frac{m^2c^4}{2p^2c^2}+...}{1-\frac{p_L}{p}+\frac{m^2c^4}{2p^2c^2}+...} \end{aligned} \tag{A.4}$$

Now from basic trigonometry it follows that $\frac{p_L}{p} = \cos\theta$. Writing out the terms $1+\frac{p_L}{p}$ and $1+\frac{p_L}{p}$ yields:

$$\begin{aligned} 1+\frac{p_L}{p} &= 1+\cos\theta = 1+(\cos^2\frac{\theta}{2}-\sin^2\frac{\theta}{2}) = 2\cos^2\frac{\theta}{2} \\ 1-\frac{p_L}{p} &= 1-\cos\theta = 1-(\cos^2\frac{\theta}{2}-\sin^2\frac{\theta}{2}) = 2\sin^2\frac{\theta}{2} \end{aligned}$$

Now substituting these expressions back in equation A.4, the pseudorapidity η is obtained.

$$\begin{aligned} y &\simeq \frac{1}{2} \ln \frac{\cos^2 \frac{\theta}{2}}{\sin^2 \frac{\theta}{2}} \\ &\simeq -\ln \tan \frac{\theta}{2} \end{aligned} \tag{A.5}$$

$$\Rightarrow \eta = -\ln \tan \frac{\theta}{2} \tag{A.6}$$

B Calibration procedure figures

This appendix section is inserted to reduce the number of figures in section 5. This section is ordered such that whenever a figure is presented in section 5, the figures belonging to other energies or quadrants will be presented here. Therefore the raw hit densities will be presented first, then the integrated hit densities and so on. The different processes are divided in subsections to display the figures more structurally.

B.1 Raw lateral hit densities

The raw lateral hit densities $\nu_{l,q}$ for different layers are shown in figure B.1 and B.2.

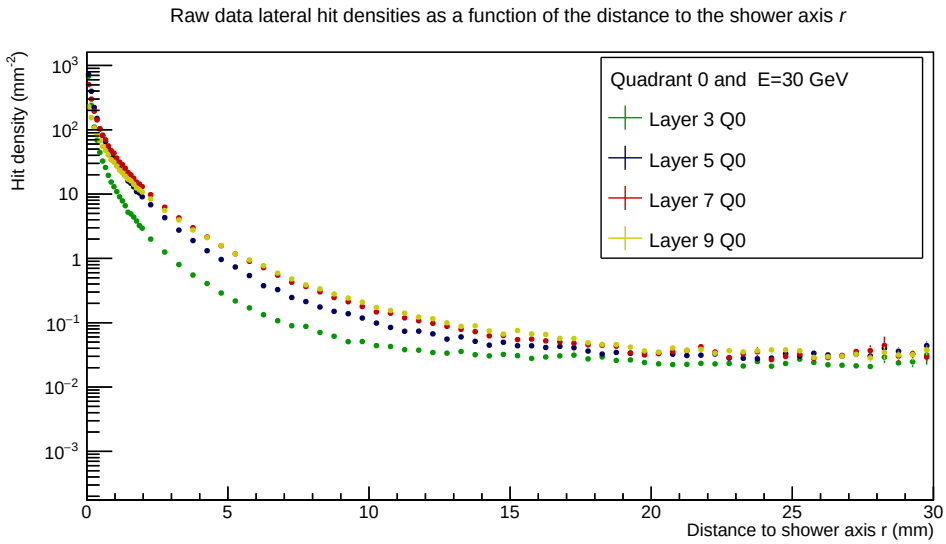

(a) $E = 30$ GeV

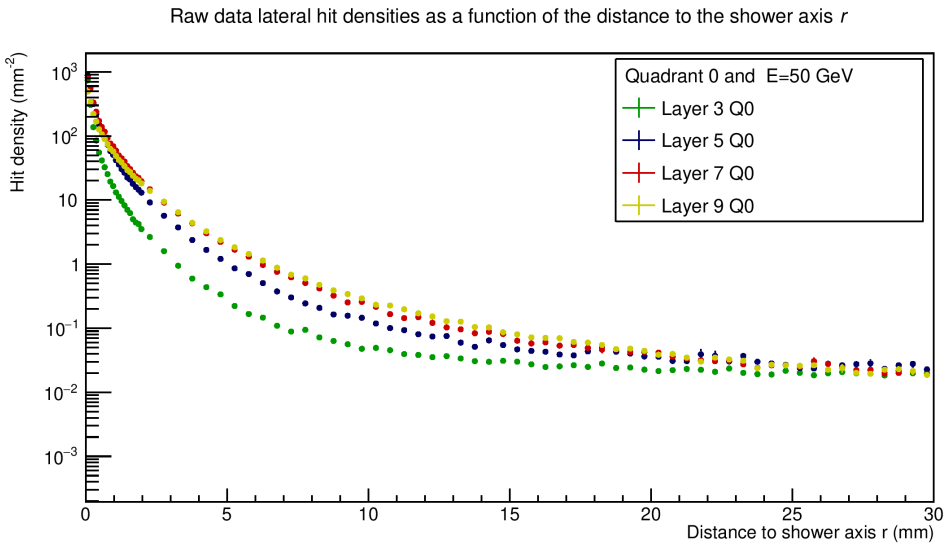

(b) $E = 50$ GeV

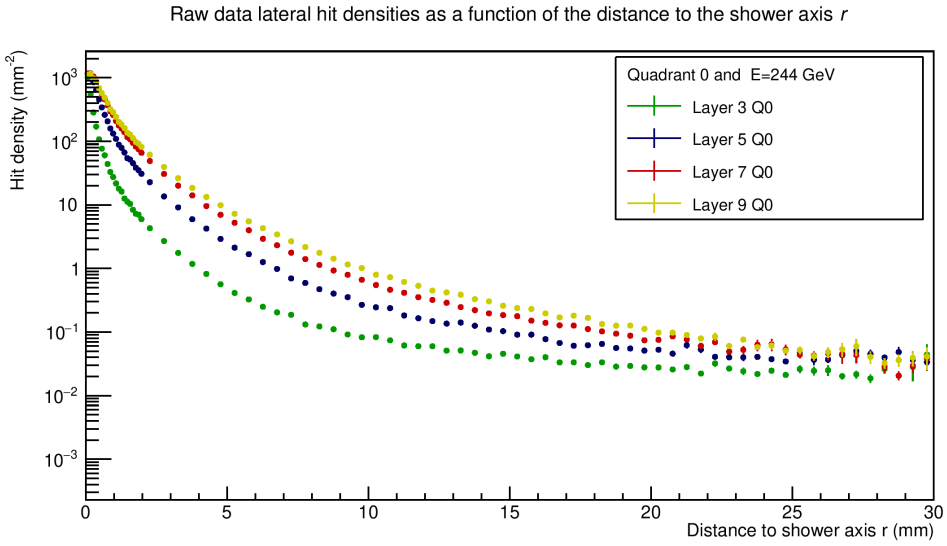

(c) $E = 244$ GeV

Figure B.1: The average lateral hit densities obtained from raw data as a function of the distance to the shower axis r for 30 GeV (a), 50 GeV (b) and 244 GeV (c). The densities are generated with data of quadrant 0 applied to equation 4.5 for four different layers:3, 5, 7 and 9.

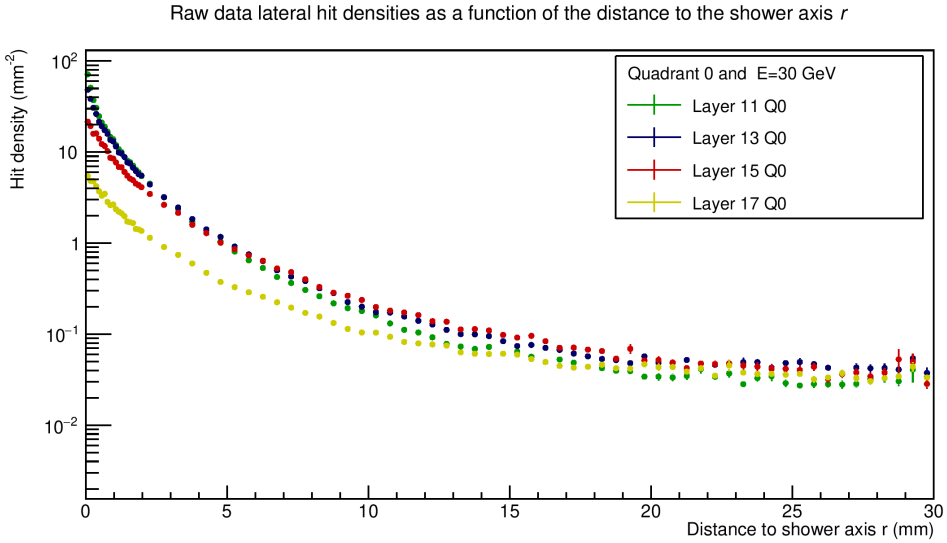

(a) $E = 30$ GeV

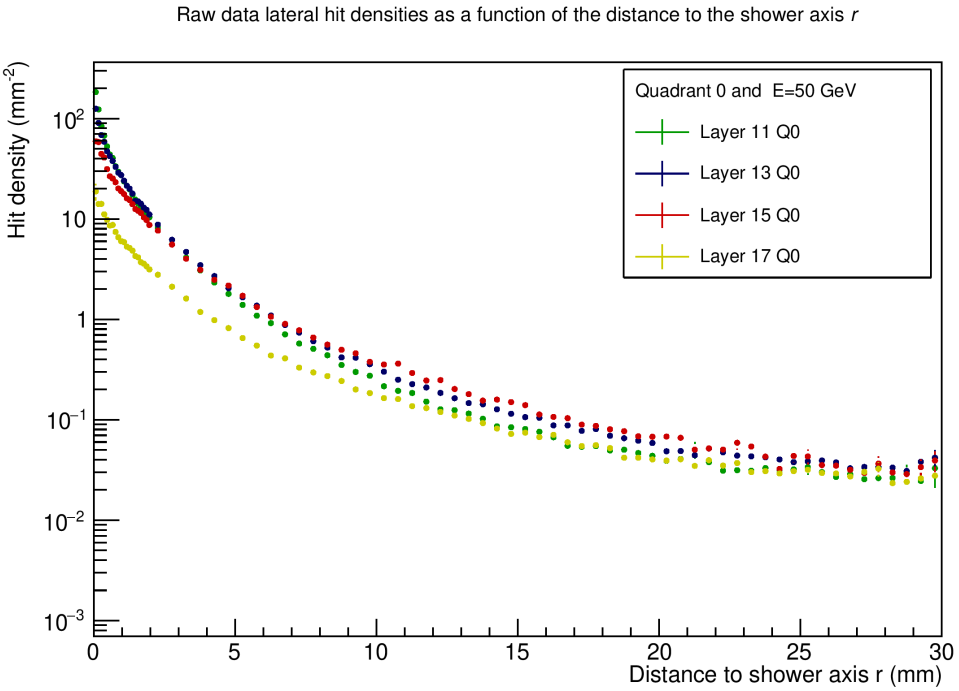

(b) $E = 50$ GeV

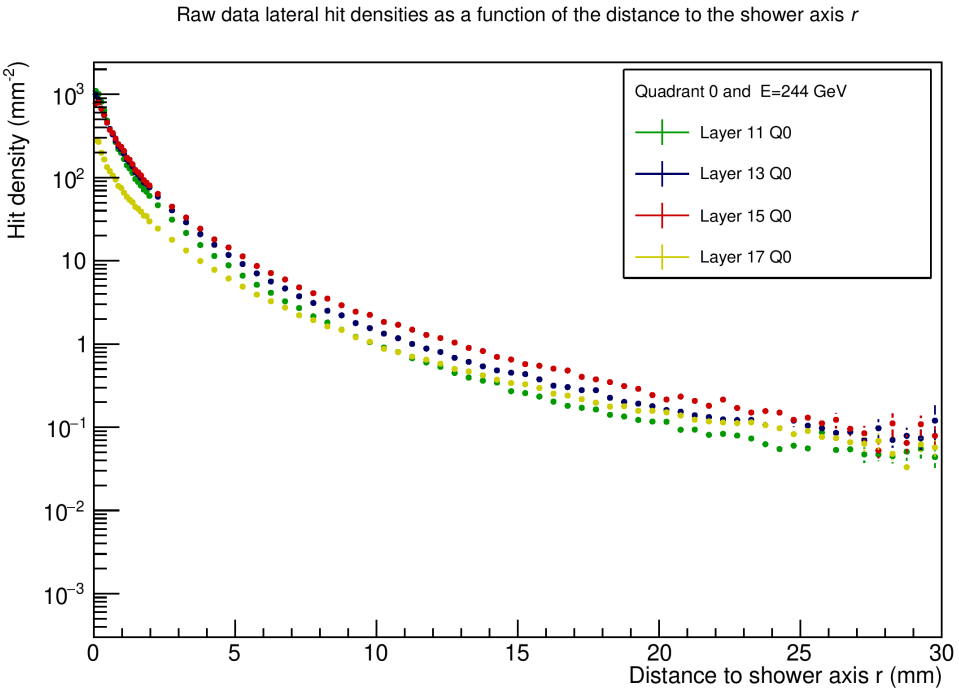

(c) $E = 244$ GeV

Figure B.2: The average lateral hit densities obtained from raw data as a function of the distance to the shower axis r for 30 GeV (a), 50 GeV (b) and 244 GeV (c). The densities are generated with data of quadrant 0 applied to equation 4.5 for four different layers:11, 13, 15 and 17.

B.2 Integrated averaged raw lateral hit density profiles $\langle \nu_{l,q} \rangle$

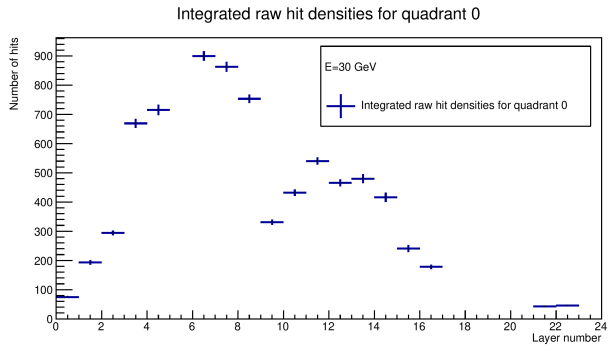

(a) Quadrant 0

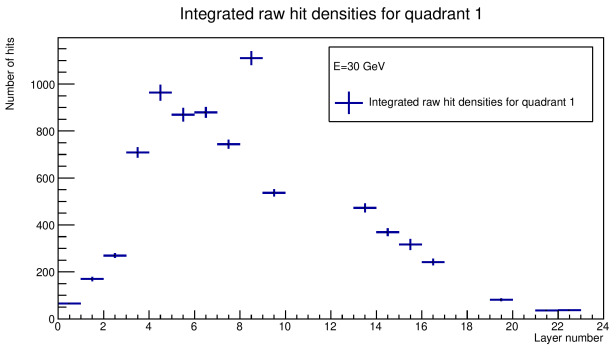

(b) Quadrant 1

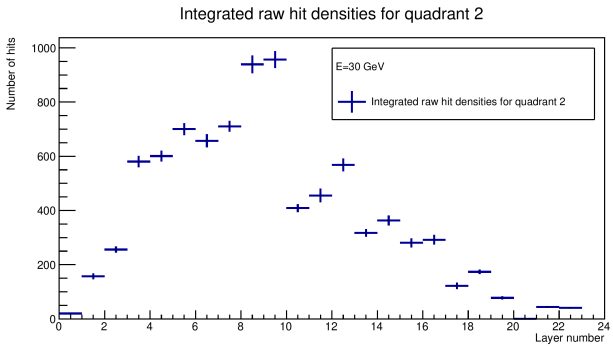

(c) Quadrant 2

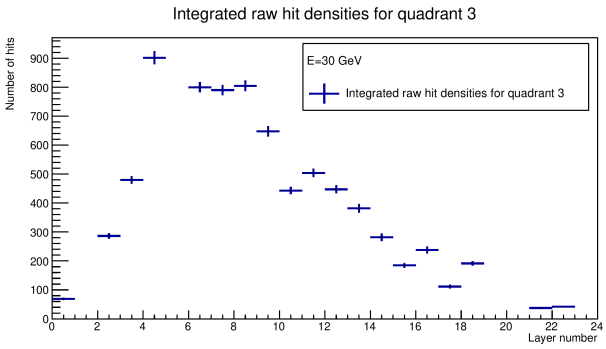

(d) Quadrant 3

Figure B.3: The raw longitudinal hit profiles for each quadrant attained by integrating the raw lateral hit densities as function of the layer number. The profiles are shown for a beam energy of a 30 GeV.

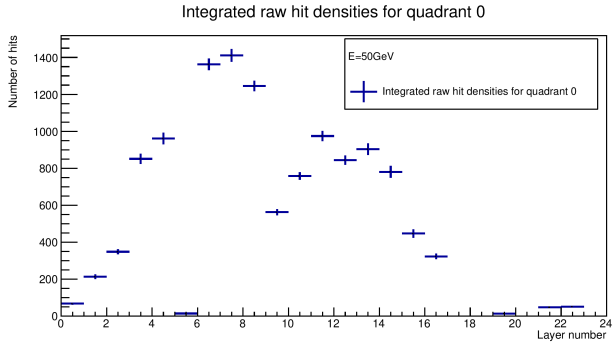

(a) Quadrant 0

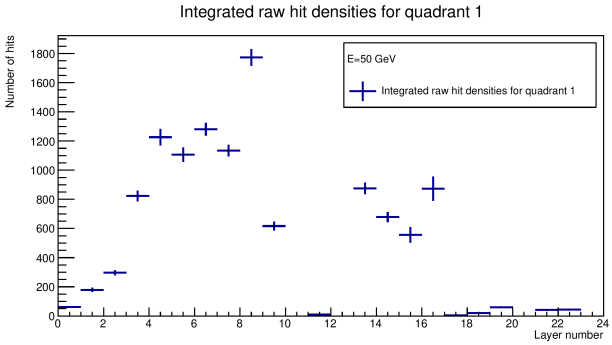

(b) Quadrant 1

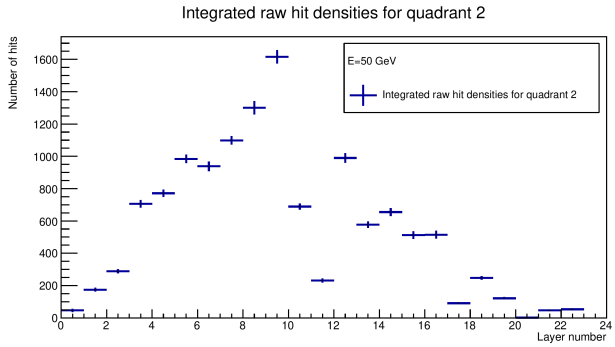

(c) Quadrant 2

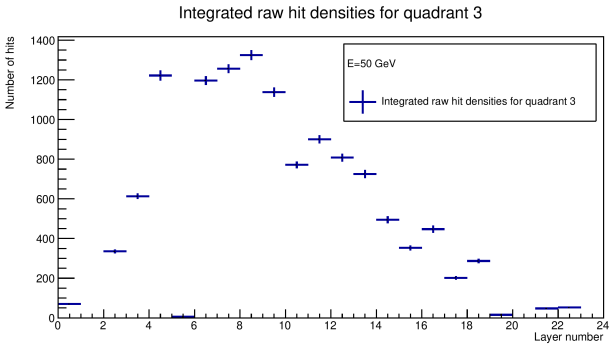

(d) Quadrant 3

Figure B.4: The raw longitudinal hit profiles for each quadrant attained by integrating the raw lateral hit densities as function of the layer number. The profiles are shown for a beam energy of a 50 GeV.

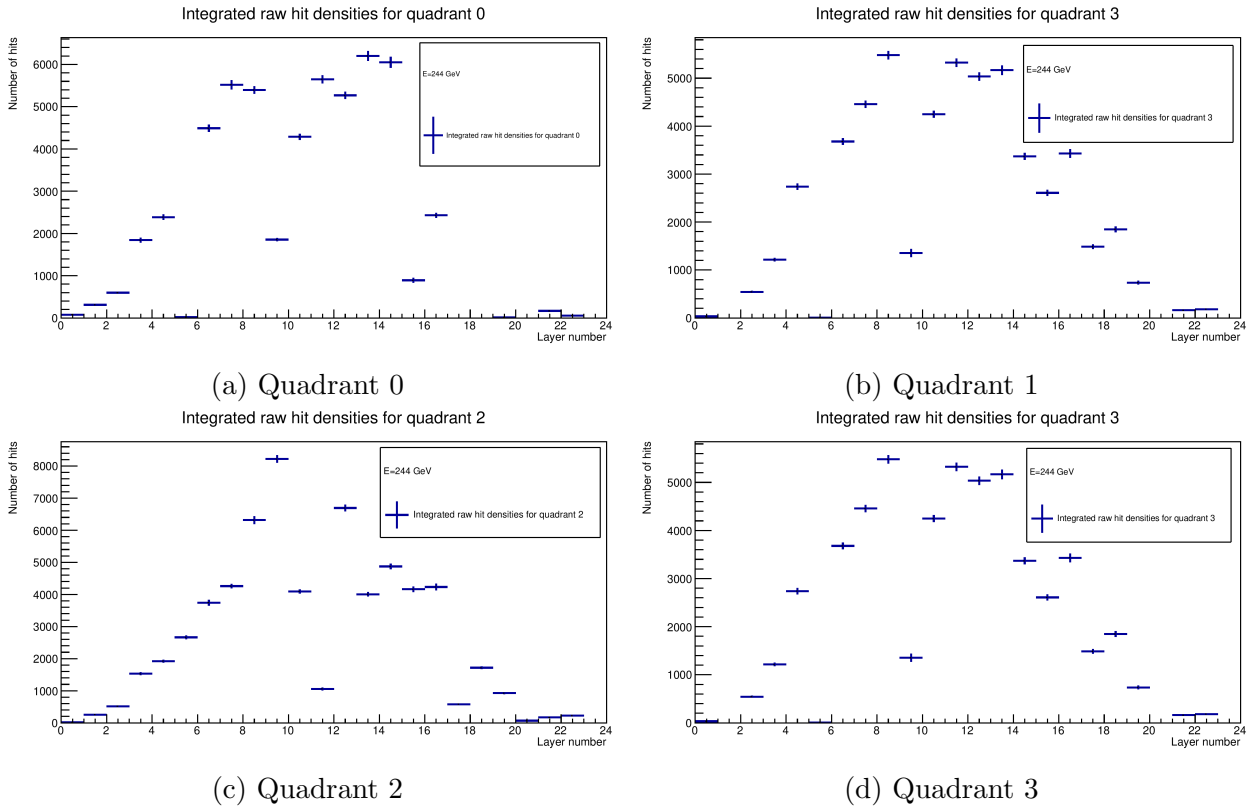

(a) Quadrant 0

(b) Quadrant 1

(c) Quadrant 2

(d) Quadrant 3

Figure B.5: The raw longitudinal hit profiles for each quadrant attained by integrating the raw lateral hit densities as function of the layer number. The profiles are shown for a beam energy of a 244 GeV.

B.3 Average hit profiles with corresponding fits

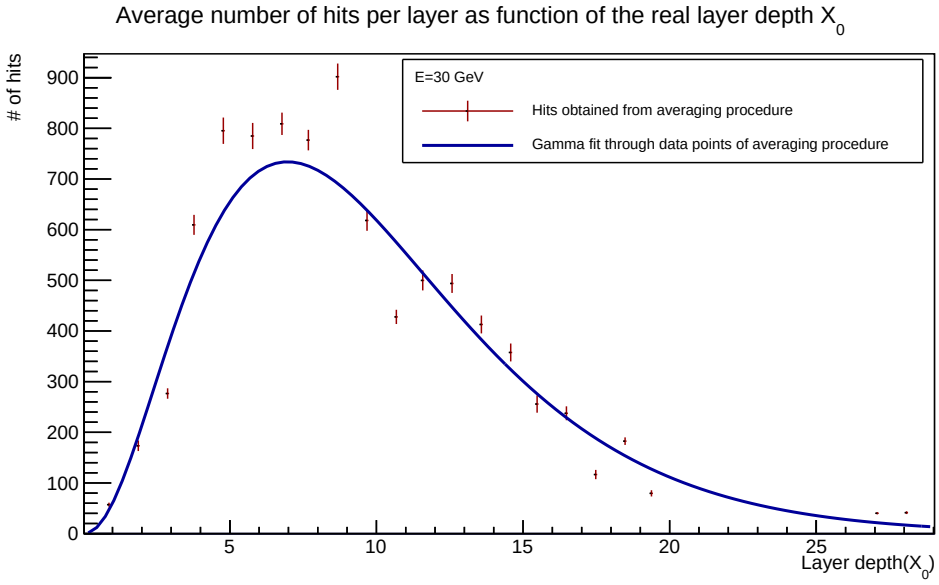

(a) $E = 30$ GeV

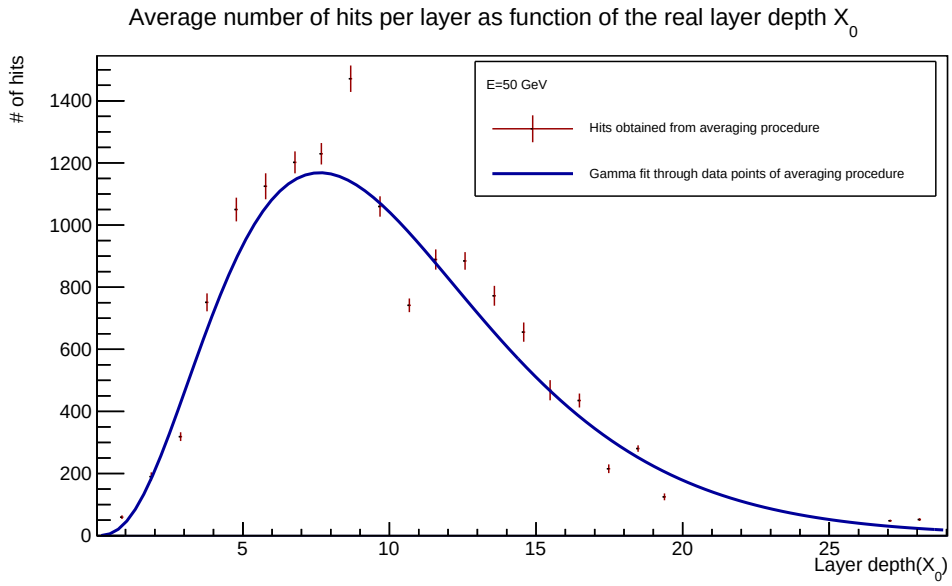

(b) $E = 50$ GeV

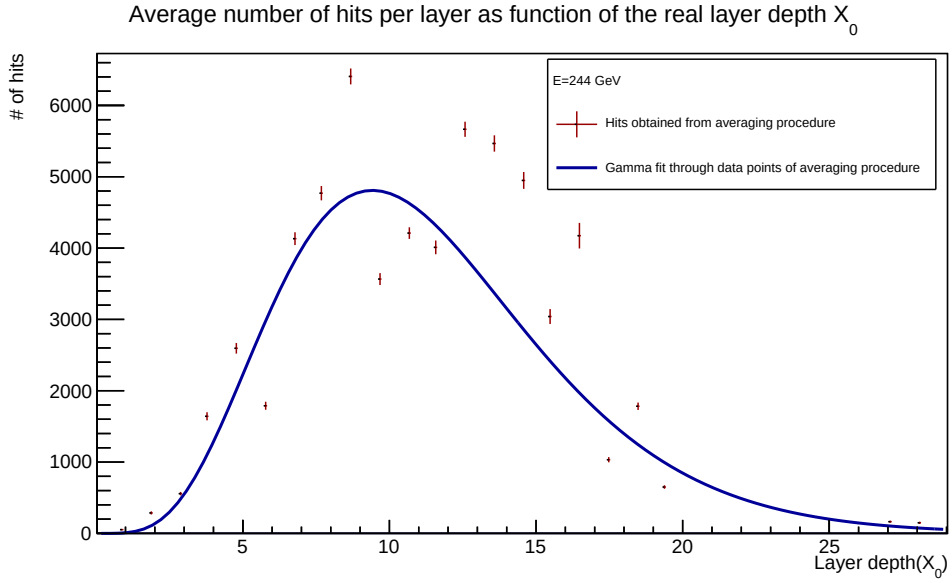

(c) $E = 244$ GeV

Figure B.6: The average number of hits per quadrant (red points) which are found by adding the number of hits in each layer for all quadrants and dividing it through the number of working chips in the layer. The gamma distribution of equation 2.10 is fitted through the data points (blue line). The average data points represent the number of hits at the real depth in the stack (X_0) of layer l. The beam energy of interest is listed below the corresponding figure.

B.4 Raw longitudinal hit profiles

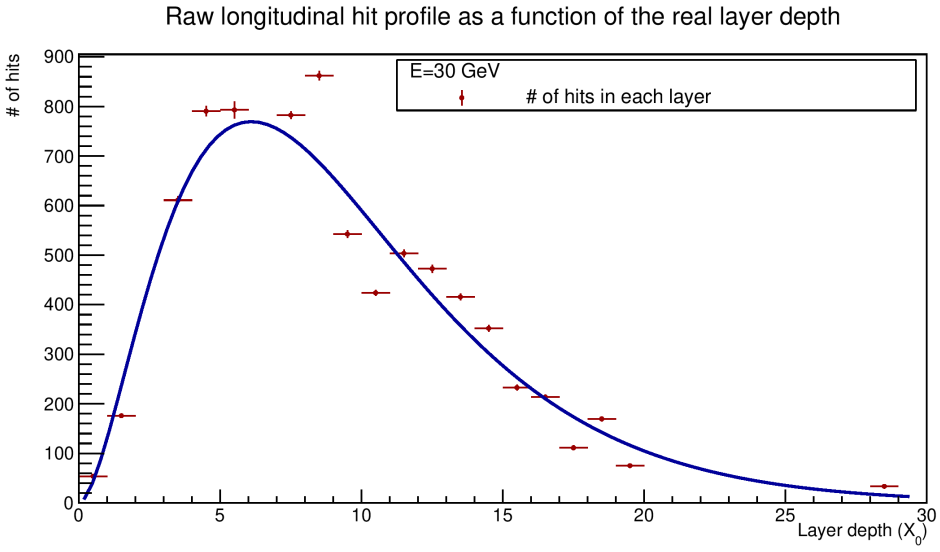

(a) $E = 30$ GeV

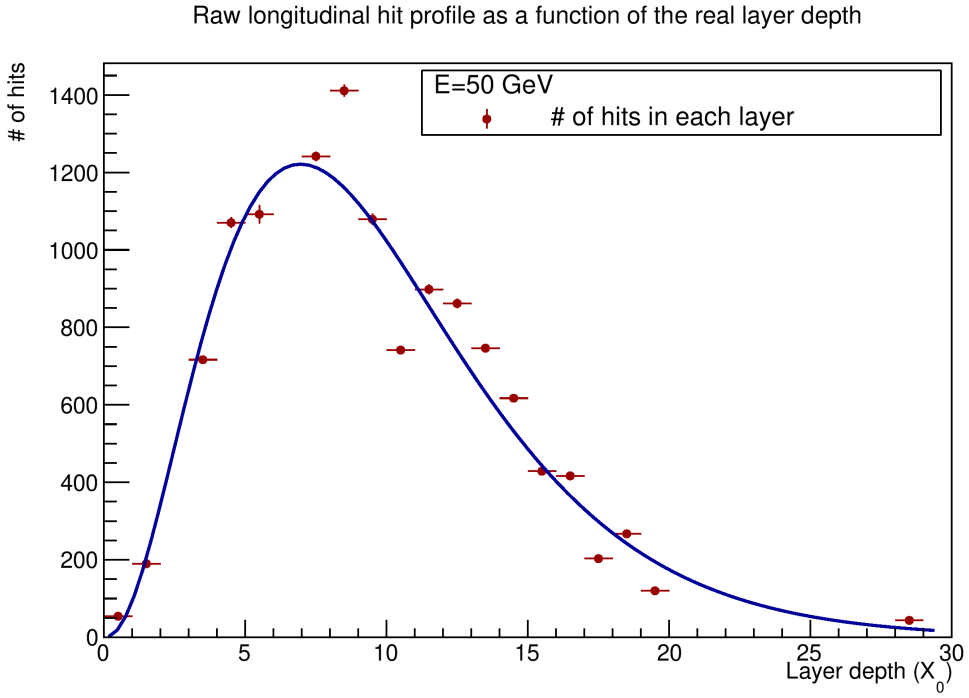

(b) $E = 50$ GeV

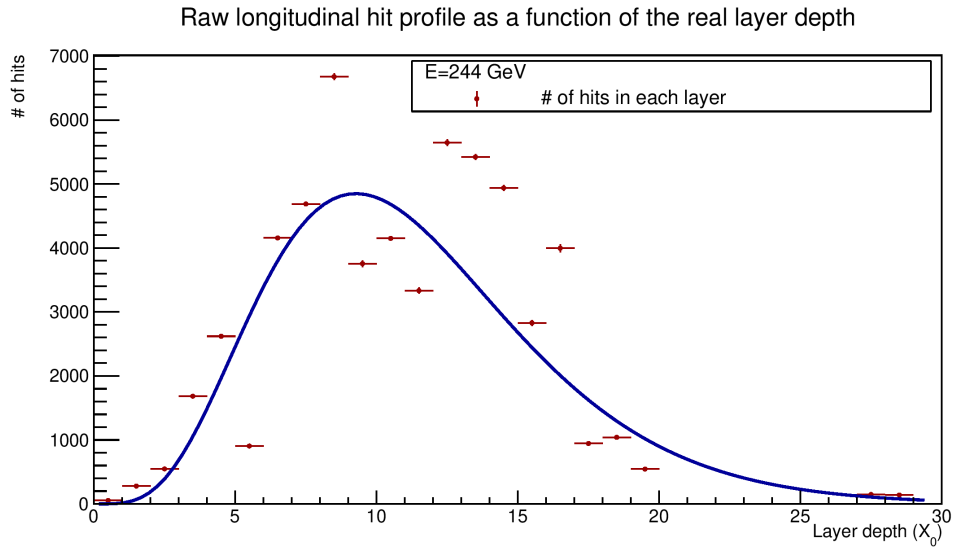

(c) $E = 244$ GeV

Figure B.7: The raw estimated number of hits using the information of the quadrants shown as a function real depth of the layer in the stack in units of X_0. The data points are shown in red. The gamma distribution of 2.10 is fitted through the data points and indicated by the blue line. The beam energy used to obtain the profiles are shown under the figures.

B.5 Calibration factors

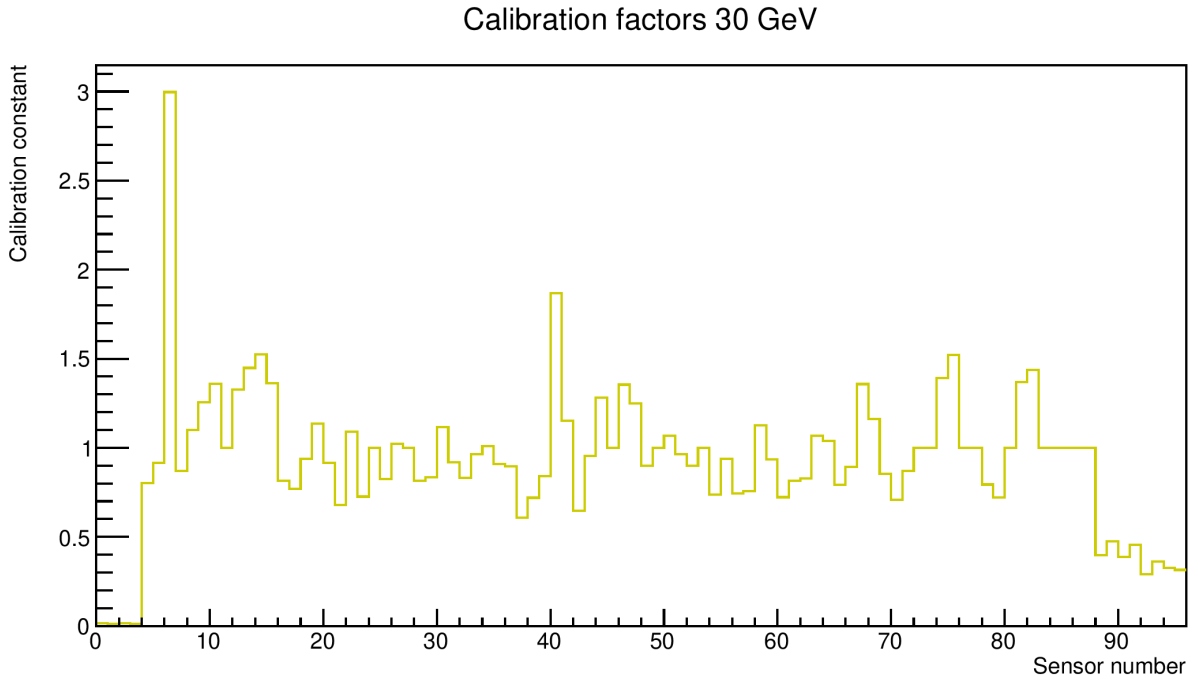

(a) Calibration factors for $E = 30$ GeV

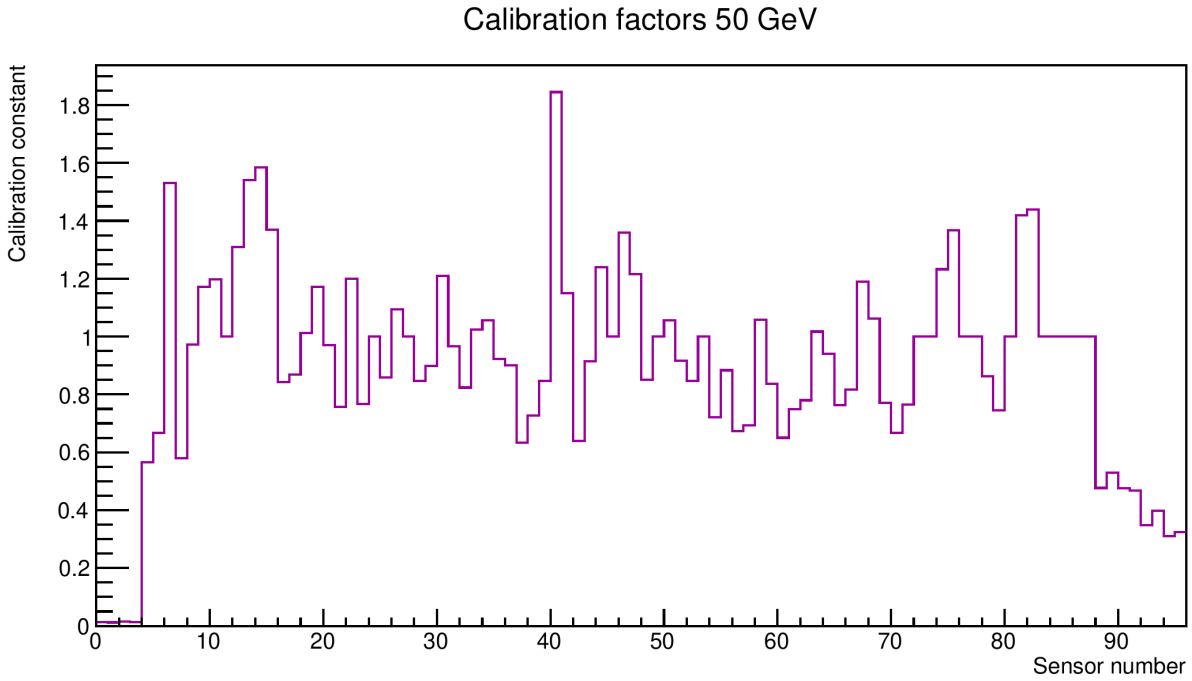

(b) Calibration factors for $E = 50$ GeV

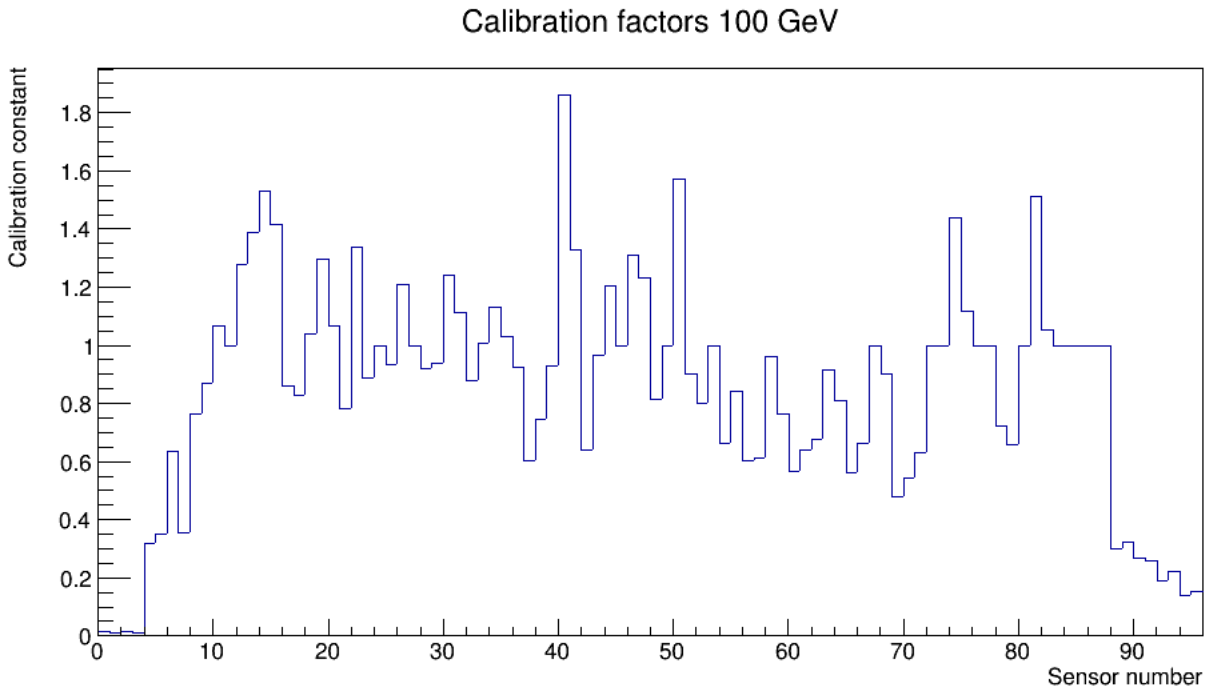

(c) Calibration factors for $E = 100$ GeV

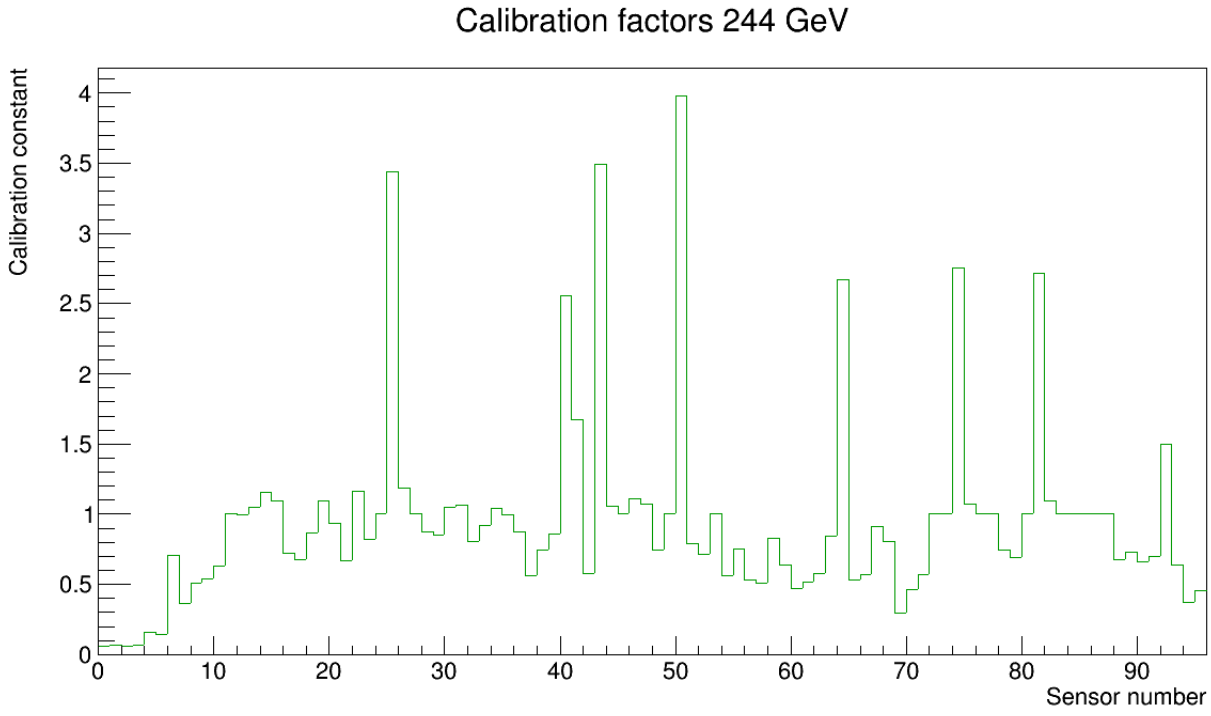

(d) Calibration factors for $E = 244$ GeV

Figure B.8: The calibration factors plotted against the sensor numbers. The figures show the calibration factors for each separate energy.

L	Q0				Q1				Q2				Q3			
E(GeV)	30	50	100	244	30	50	100	244	30	50	100	244	30	50	100	244
1	0.014	0.014	0.014	0.060	0.012	0.012	0.012	0.071	0.014	0.014	0.013	0.059	0.013	0.013	0.012	0.064
2	0.801	0.565	0.317	0.156	0.917	0.667	0.350	0.146	2.997	1.531	0.636	0.710	0.869	0.580	0.353	0.364
3	1.100	0.972	0.764	0.513	1.254	1.173	0.869	0.540	1.359	1.199	1.068	0.627	1	1.	1	1
4	1.326	1.309	1.277	0.998	1.449	1.541	1.390	1.046	1.525	1.585	1.531	1.156	1.363	1.370	1.418	1.097
5	0.814	0.842	0.859	0.722	0.769	0.869	0.826	0.674	0.939	1.012	1.040	0.869	1.135	1.172	1.296	1.096
6	0.915	0.970	1.066	0.939	0.679	0.757	0.783	0.672	1.090	1.200	1.337	1.165	0.726	0.766	0.889	0.818
7	1	1	1	1	0.824	0.859	0.936	3.441	1.022	1.094	1.207	1.183	1	1	1	1
8	0.816	0.846	0.917	0.872	0.835	0.899	0.938	0.849	1.117	1.209	1.239	1.046	0.918	0.966	1.112	1.064
9	0.831	0.824	0.877	0.806	0.965	1.023	1.007	0.919	1.010	1.056	1.131	1.044	0.908	0.922	1.030	0.998
10	0.897	0.900	0.925	0.874	0.609	0.633	0.604	0.559	0.720	0.728	0.745	0.746	0.840	0.846	0.928	0.860
11	1.868	1.845	1.861	2.553	1.153	1.150	1.329	1.670	0.647	0.640	0.642	0.576	0.956	0.914	0.967	3.500
12	1.282	1.240	1.206	1.060	1	1	1	1	1.354	1.360	1.311	1.110	1.250	1.216	1.233	1.070
13	0.899	0.850	0.815	0.745	1	1	1	1	1.067	1.056	1.574	3.978	0.964	0.916	0.899	0.791
14	0.901	0.846	0.800	0.718	1	1	1	1	0.738	0.721	0.661	0.565	0.938	0.884	0.842	0.751
15	0.745	0.673	0.605	0.534	0.756	0.693	0.611	0.510	1.127	1.058	0.962	0.827	0.935	0.836	0.761	0.641
16	0.723	0.650	0.566	0.468	0.815	0.750	0.638	0.515	0.829	0.780	0.678	0.581	1.067	1.018	0.915	0.841
17	1.040	0.941	0.809	2.668	0.792	0.763	0.562	0.528	0.893	0.817	0.662	0.571	1.358	1.190	0.997	0.912
18	1.162	1.063	0.901	0.807	0.855	0.771	0.478	0.297	0.709	0.668	0.544	0.463	0.870	0.765	0.631	0.572
19	1	1	1	1	1	1	1	1	1.392	1.233	1.436	2.751	1.521	1.368	1.116	1.072
20	1	1	1	1	1	1	1	1	0.794	0.862	0.722	0.744	0.721	0.746	0.658	0.692
21	1	1	1	1	1.368	1.420	1.512	2.718	1.437	1.440	1.054	1.091	1	1	1	1
22	1	1	1	1	1	1	1	1	1	1	1	1	1	1	1	1
23	0.397	0.478	0.299	0.675	0.475	0.531	0.323	0.728	0.389	0.476	0.269	0.660	0.455	0.468	0.260	0.703
24	0.291	0.349	0.188	1.496	0.360	0.400	0.220	0.638	0.327	0.310	0.137	0.370	0.314	0.324	0.151	0.458

B.6 Calibrated lateral hit densities

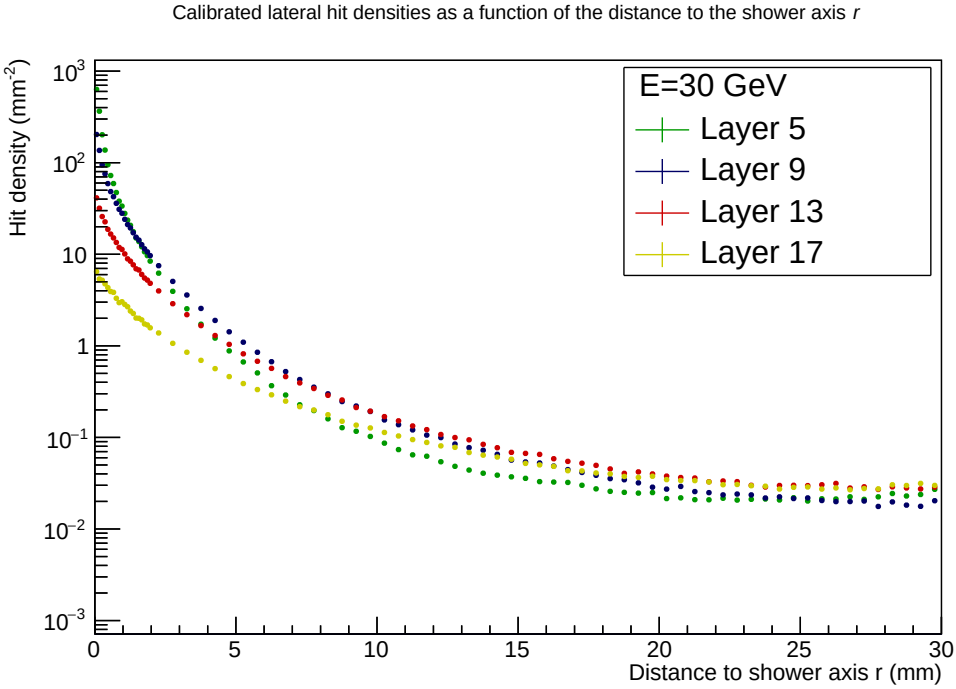

(a) $E = 30$ GeV

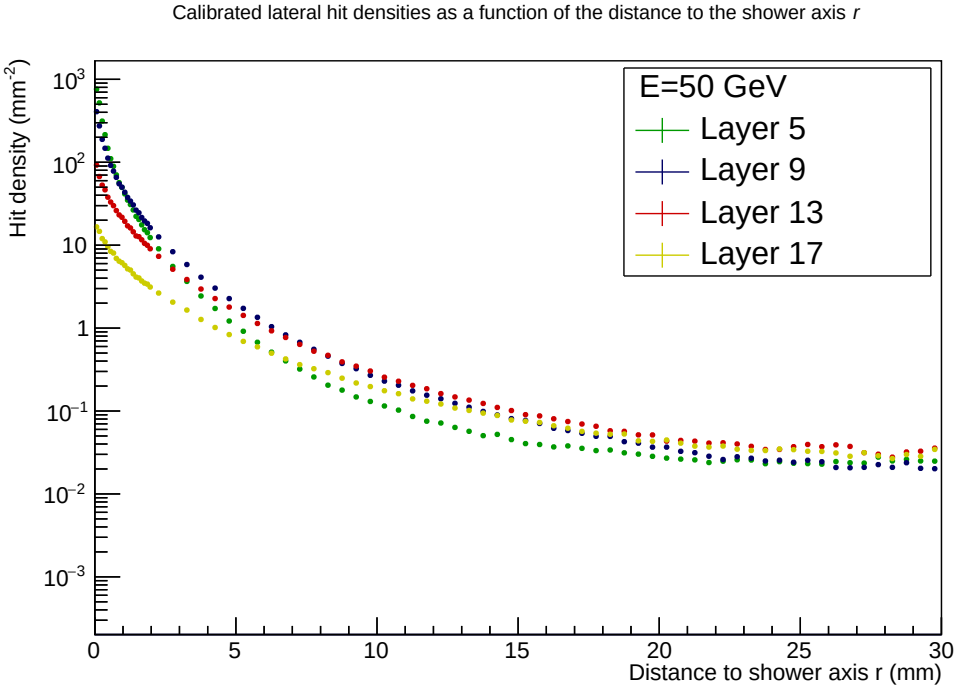

(b) $E = 50$ GeV

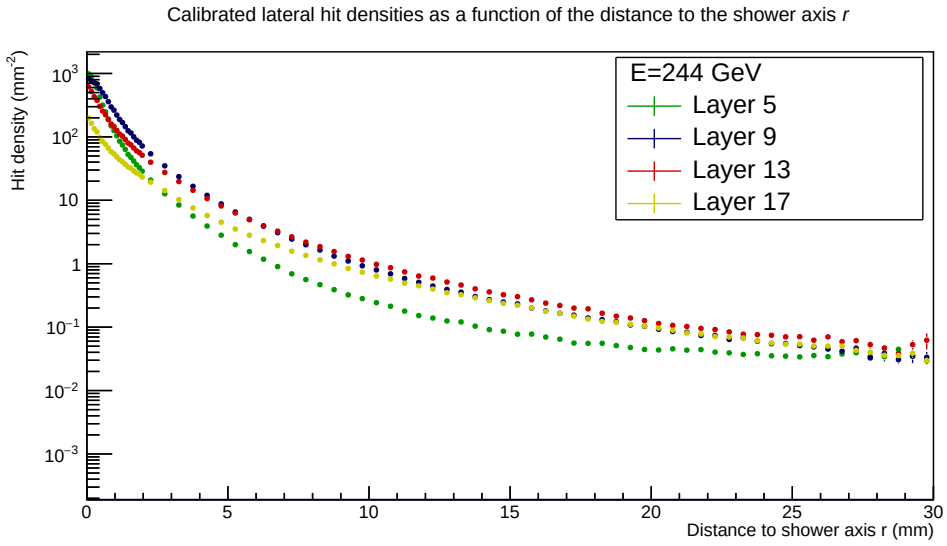

(c) $E = 244$ GeV

Figure B.9: The average lateral hit densities obtained from calibrated data as a function of the distance to the shower axis r. The densities are generated with data of quadrant 0 applied to equation 4.12 for four different layers:3, 5, 7 and 9. The energy of the beam particles used are listed below the figures

B.7 Calibrated longitudinal profiles with corresponding fit

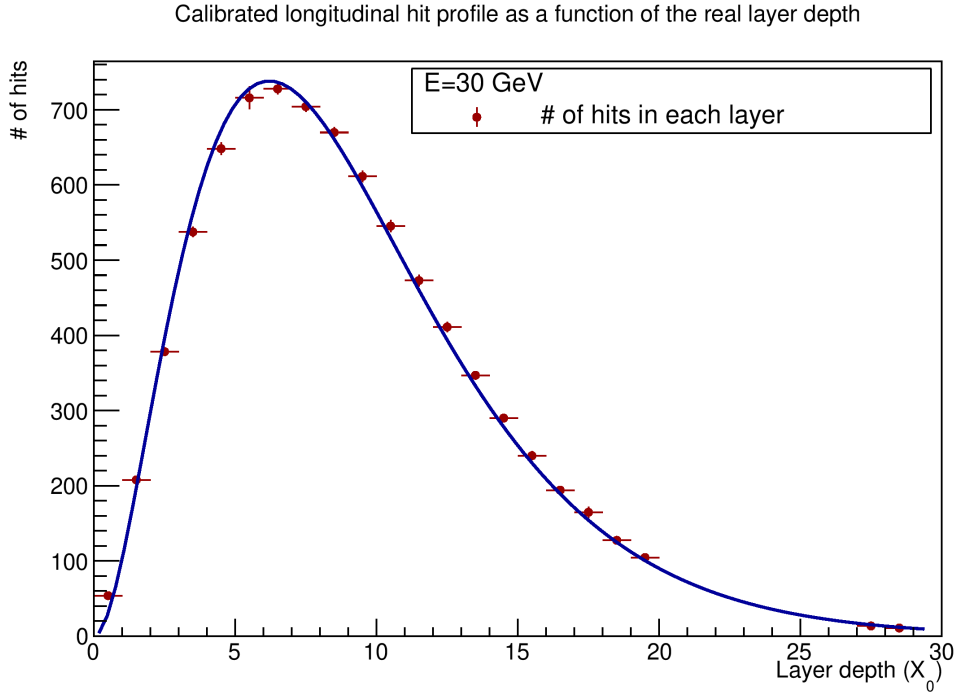

(a) $E = 30$ GeV

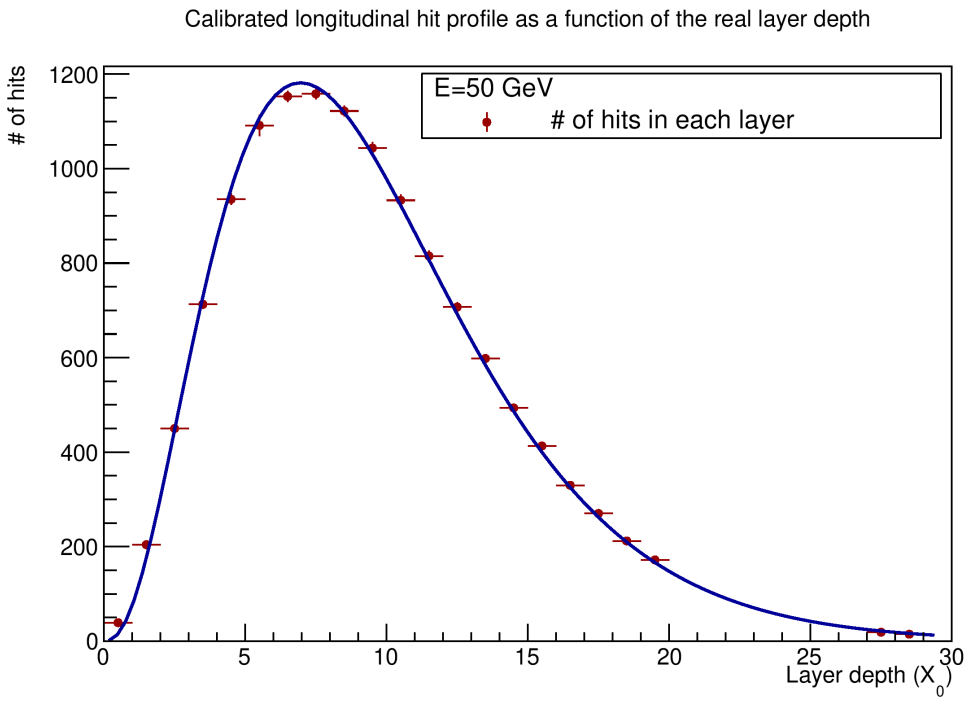

(b) $E = 50$ GeV

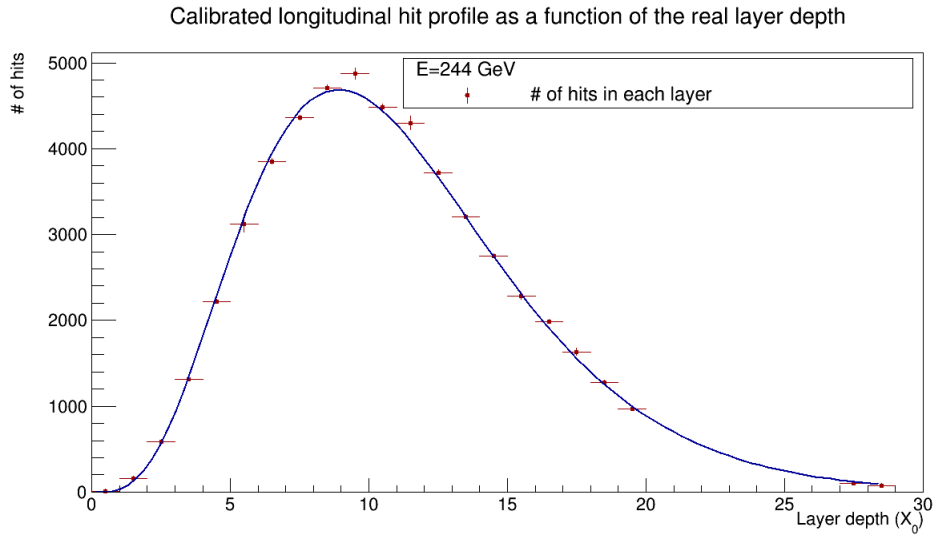

(c) $E = 244$ GeV

Figure B.10: The longitudinal hit profiles obtained by calibrating the raw data, as function of the real layer depth in units of X_0 (red points). The gamma distribution of equation 2.10 is fitted through the longitudinal profile (blue line). The beam energy of interest is shown under the figures.

C Data runs

C.1 Good runs

Beam Energy (GeV)	Data runs
244	30, 32, 34, 36, 38, 42, 44, 46, 47, 49, 51, 53, 55
100	75, 81, 82, 84, 87, 89, 95, 96, 98, 100, 102, 104, 106, 108, 110, 112, 114, 116, 117, 128, 130, 131, 132, 134, 136, 138, 140, 142, 145, 146, 149, 150, 156, 157, 158, 162, 163, 164, 165, 167, 169, 170, 171, 173, 175, 177, 179, 181, 183, 185, 187, 189, 190, 192, 194, 195
50	196, 198, 200, 201, 202, 204, 208, 209, 211, 213, 215, 217, 219, 221, 223, 225, 227
30	229, 230, 231, 233, 235, 237, 239, 240, 242, 244, 246, 248, 250, 252, 253, 255

C.2 Pedestal runs

Beam Energy (GeV)	Data runs
244	28, 31, 33, 35, 37, 39, 41, 43, 45, 48, 50, 52, 54, 56
100	83, 85, 86, 88, 90, 91, 93, 94, 97, 99, 101, 103, 105, 107, 109, 111, 113, 115, 127, 129, 135, 137, 139, 141, 143, 147, 148, 159, 161, 166, 168, 172, 174, 176, 178, 180, 182, 184, 186, 188, 191, 193
50	197, 199, 203, 205, 207, 210, 212, 214, 216, 218, 220, 222, 224, 226
30	228, 232, 234, 236, 238, 241, 243, 245, 247, 249, 251, 254, 256

D Instructions manual FoCal group cluster

The data taken at CERN SPS and at DESY has to be processed and analysed. This analysis is done with ROOT, which executes C++ code. Before the instructions on how to use ROOT, it is important to gate into the FoCal group cluster: Quark. To enter the Quark cluster, open a terminal and fill in the following line:

- Gate into Quark on a computer at the university or university library: ssh -X -Y (student number)@quark.science.uu.nl
- Gate into Quark on an own device or a device not connected to Utrecht University Eduroam: ssh -X -Y (student number)@gemini.science.uu.nl. After gating into gemini, the Quark cluster can be entered by filling in the line: ssh -X -Y (student number)@quark.science.uu.nl

After filling in the line to gate into Quark, a password is required. This password is the Solis-ID password. Some usefull shortcuts in the cluster terminal are:

- pwd : shows the directory in which you are located.
- $\sim$: the tilde directory is your home directory.
- cd /directory: the cd command brings you to the directory which you type after the /.
- cd .. : the cd .. command brings you one directory back.
- (s)cp : (s)cp can be used to (secure) copy files to your own directory. For example:(s)cp file.C /nethome/studentnumber/. To copy a whole directory, -r has to be added after the cp statement.
- rm: rm command removes files. rmdir removes a whole directory.
- mkdir: the mkdir command makes a new directory. The name of the directory is specified after the mkdir statement.

As can be read in the Quark cluster instructions [24], the file .bashrc has to be copied to the home directory. Using the shortcuts above, this is obtained by typing the following line in the terminal: scp .bashrc (student number)@quark.science.uu.nl:$\sim$ (note: the terminal should be in its local environment, so not logged in on Quark). Now by adding the following lines to the .bashrc file (or just copying them to the terminal), access to ROOT will be achieved [24]:

- module load python/2.7
- export PATH=/cm/local/apps/environment-modules/3.2.10/Modules/3.2.10/bin/:$PATH
- export ALIBUILD_WORK_DIR=/data1/software/alisoft
- alienv enter –shellrc AliPhysics/latest-master-root6

If too many large ROOT jobs are running in the terminal, the swap memory of the Quark cluster might be occupied by these jobs. To get rid of this problem, the command qsub is used. To use the qsub command a bash script has to be written. This bash script contains the lines that would have typed in the terminal when using ROOT. To submit the job (i.e. running your script), type the following in the terminal:

- qsub -V -cwd (your bash script)

The job is now submitted and will be run in one of the 48 job slots of the Quark cluster. To check on the status of the job that has been submitted, type the command "qstat" in the terminal.

E Instructions manual for the calibration procedure

The calibration procedure has been coded in C++ using the text editor GNU Emacs. The file which contains the calibration procedure code is called FOCALDensityProfiles.C. The FOCALDensityProfiles.C file makes use of several C++ classes, which have to be loaded. After the ROOT environment has been set, the C++-files necessary for the FOCALDensityProfiles.C file are loaded in by typing the following line in the terminal:

- root -l LoadEverything.C (The LoadEverything.C file contains all the files the FOCALDensityProfiles.C needs.)

The ROOT environment has been entered and the FOCALDensityProfiles.C file can be attained by typing:

- FOCALDensityProfiles f

By typing the line above, ROOT checks immediately if the required directories to store the ROOT files are present and if they are not, it creates them.

The calibration procedure is coded in different steps using different functions. The functions will be discussed in the order as they appear in the calibration procedure.

f.ShowerPropertiesLoopOverRuns(StartRun, StopRun):
The ShowerPropertiesLoopOverRuns function creates ROOT files where for a run all the frames with a good event are stored. The properties of the event stored in the file are:

- frame number
- position of the incoming beam particles (shower axis)
- hits per layer
- clusters per layer

The file created per run is called DensityRun[#].root, where the # indicates the run number. The file is stored in the directory DensityRun/SPS/$E\_GeV/$ where the # indicates the run number and E the energy of the incoming beam particles. Running this function takes a lot of time and swap memory, so it is convenient to submit this function as a job using qsub.

f.ReadAllDensity(StartRun,StopRun, Calibration, Noise):
The ReadAllDensity function generates the lateral hit densities. In the header of the function it is possible to generate lateral hit densities with or without noise included. Furthermore it is possible to generate calibrated and uncalibrated lateral hit densities. The noise variable is set as:

- with noise subtracted: Noise = 0
- without noise subtracted: Noise = 1

The calibration variable is set as:

- raw lateral hit densities: Calibration = 0
- calibrated lateral hit densities: Calibration = 1

The ReadAllDensity function creates 5 ROOT files, which are of the form:

- Raw: RawRun(StartRun)(StopRun)RadialProfile_Quadrant_#_NoNoise_ChunhuiData_DistanceToEd
- Calibrated: CorrectedRun(StartRun)(StopRun)RadialProfile_Quadrant_#_NoNoise_ChunhuiData_D

The function creates a file for each quadrant and one for the total longitudinal profile. Each file contains 24 histograms which show the lateral hit densities for each layer and they are called Layer_#, where the # indicates the layer number. The files are stored in /Densities/SPS/

f.LoopUncalibratedQuadrants(StartRun, StopRun, Noise)
The function LoopUncalibratedQuadrant generates the raw longitudinal hit profiles for each quadrant and generates the total raw longitudinal profile. The function creates a file of the form:

- Run(StartRun)(StopRun)RawLongitudinalProfile_NoNoise_ChunhuiData_DistanceToEdgeSelection_5

This file contains 5 histograms indicated by Q_#, where # indicates the number of the quadrant. # equals -1 for the longitudinal profile. The file is stored in /Densities/SPS/.

f.GiveMeCalibrationFactors(StartRun,StopRun,Noise):
The function GiveMeCalibrationFactors generates the calibration factors for the energy belonging to the runs filled in the function. The function inside the GiveMeCalibrationFactors that takes care of the averaging procedure is called GetReferenceFit(StartRun,StopRun). The function that takes care of calculating the calibration factors is called CreateFactors(StartRun, StopRun).GiveMeCalibrationFactors creates a file called chipfactors_E.root, where E is equal to the beam energy of the incoming particles, which is directly obtained by reading out the run numbers. The file is stored in /codeForCorrection_Chunhui.

f.LoopcalibratedQuadrants(StartRun, StopRun, Noise):
LoopCalibratedQuadrants generates the calibrated longitudinal profile for each quadrant and the total calibrated longitudinal profile. The function creates a file called:

- Run(StartRun)-(StopRun)CorrectedLongitudinalProfile_NoNoise_DistanceToEdgeSelection_5mm.roo

The file contains 5 histograms indicated by Q_#, where # indicates the number of the quadrant. # equals -1 for the longitudinal profile. The file is stored in /Densities/SPS/.

The perform the calibration procedure with all the runs taken into account, the following has to be followed for the SPS data:

- 30 GeV: StartRun = 229, StopRun = 255
- 50 GeV: StartRun = 198, StopRun = 223

- 100 GeV: StartRun = 81, StopRun = 195
- 244 GeV: StartRun = 30, StopRun = 55

To run the whole calibration procedure for a 100 GeV beam such that in the end calibrated longitudinal profiles are obtained, follow the steps below:

- ROOT -l LoadEverything.C
- FOCALDensityProfiles f
- f.ShowerPropertiesLoopOverRuns(81,195)
- f.ReadAllDensity(81,195,0,0)
- f.GiveMeCalibrationFactors(81,195,0)
- f.ReadAllDensity(81,195,1,0)
- f.LoopCalibratedQuadrants(81,195,0)